Graz University of Technology
Institute of Applied Mechanics

AM:BM

Preprint Series

Preprint No 02/2019

A coupled FEM-MFS method for the vibro-acoustic simulation of laminated poro-elastic shells

Michael H Gfrerer
Institute of Applied Mechanics, Graz University of Technology

Martin Schanz
Institute of Applied Mechanics, Graz University of Technology

This is a post-peer-review, pre-copyedit version of the article published in *International Journal for Numerical Methods in Engineering*, 121 (19), 4235–4267, 2020

The final authenticated version is available online at: https://doi.org/10.1002/nme.6391

Abstract

A new simulation method for the vibro-acoustic simulation of poro-elastic shells is presented. The proposed methods can be used to investigate arbitrary curved layered panels, as well as their interaction with the surrounding air. We employ a high order finite element method (FEM) for the discretization of the shell structure. We assume that the shell geometry is given parametrically or implicitly. For both cases the exact geometry is used in the simulation. In order to discretize the fluid surrounding the structure, a variational variant of the method of fundamental solutions (MFS) is developed. Thus, the meshing of the fluid domain can be avoided and in the case of unbounded domains the Sommerfeld radiation condition is fulfilled. In order to simulate coupled fluid-structure interaction problems, the FEM and the MFS are combined to a coupled method. The implementation of the uncoupled FEM for the shell and the uncoupled MFS is verified against numerical examples based on the Method of Manufactured Solutions. For the verification of the coupled method an example with a known exact solution is considered. In order to show the potential of the method sound transmission from cavities to exterior half-spaces is simulated.

1 Introduction

In order to reduce noise levels which are harmful for the human health, lightweight poro-elastic materials are often used in a wide range of applications such as building acoustics, automotive and aircraft interior noise. Typically, porous materials used as dissipative components are introduced in multi-layered structures. This is the motivation to develop a new simulation method, where a laminated shell structure made of elastic and poro-elastic materials is discretized by the finite element method (FEM) and the surrounding fluid is discretized by the method of fundamental solutions (MFS). In particular we focus on situations as illustrated in Figure 1. We assume that the upper half-space has a sound hard ground and is divided into an bounded interior domain and an unbounded exterior domain by a shell structure. Our main focus is to develop a simulation method in order to calculate the sound transmission from the interior to the exterior domain.

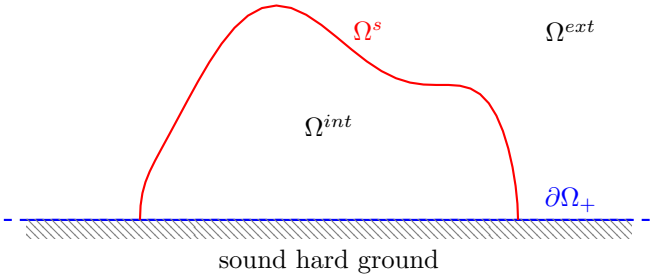

Figure 1: Problem setting: Sound hard ground surface $\partial\Omega_+$, interior fluid domain Ω^{int}, exterior fluid domain Ω^{ext}, shell structure Ω^s

The modeling of the vibro-acoustic behavior of systems including porous materials is far from being trivial. Due to the fact that in most applications only small vibration amplitudes occur, it is usual to use linear models. Therefore, air volumes are modeled with the acoustic fluid, whereas solid structures are modeled with the linearized theory of elasticity. Poro-elastic materials are described with the dynamic Biot theory. This theory was published in [6, 7] and has been adapted to acoustic applications. Present-day descriptions can be found in [2] and [19].

Many structural parts can be classified as of shell-type. Their thickness is very small when compared to the other dimensions. In such a situation, it is reasonable to describe the geometry by a curved two-dimensional surface in space. A recent review of laminated plate and shell models is given in [13]. In principle, two types of theories can be distinguished. In the first type the number of parameters is independent of the number of layers. Such theories are termed equivalent single layer theory. The second type referred to as layer-wise theories, where the number of parameters depends on the number of layers. Such a theory is formed by packages of single-layer shell models coupled at the layer interfaces. Concerning the literature on poro-elastic plate and shell theories, we mention the thin poro-elastic plate theory for the consolidation problem [63]. This theory has been extended to the dynamic problem in [64]. In [60], the displacement kinematics are extended to allow for shear deformations. Following the idea of a three-dimensional resolution, a series expansion in thickness direction by means of monomials has been utilized for single layer poro-elastic plates in [43]. This approach has been extended to

layered panels in [44], utilizing a layer-wise modeling. In this approach possible air layers can also be considered [55]. A rigorous derivation of poro-elastic plate and shell theories have been published only recently [39, 41].

The FEM is the most popular numerical discretization method for the analysis of shell structures. Due to the geometry, various locking phenomena can occur. To overcome this issue, a huge number of different techniques have been developed. In order to resolve the locking issues, many finite elements are based on mixed variational formulations. Common techniques are Reduced Integration, Assumed Natural Strains, Enhanced Assumed Strains, and the Discrete Strain Gap method (cf. [36, 70, 15]). Another possibility is the use a high order ansatz functions to reduce the locking effects [23, 51]. Typically, the geometry of the shell reference surface is approximated. However, in the present work, we make use of the exact geometry descriptions within the FEM. For the case of a parametrized surface we mention [4, 50, 29], whereas in [20, 27, 29] exact geometry methods for implicitly defined surfaces have been developed. The FE discretization of poro-elastic media can *e.g.* be found in [2]. For sophisticated solution techniques of the coupled poro-elastic system we refer to [42] and [11].

We assume that in the geometry definition of a problem only the shell geometry structure is modeled directly. The geometry of the fluid domains is described indirectly by their boundary, *i.e.* by the boundary of the half-space and the shell structure. In such a situation it can be a rather difficult task to generate a volume mesh. To tackle this problem, one possibility is to use embedded/fictitious domain methods. These methods are based on the idea of defining an auxiliary domain which can be meshed easily. As recent contributions in this field, we would like to mention the Finite Cell method [49, 58], the Cartesian grid method [40] and the CutFEM [12]. Recent developments in the context of Constructive Solid Geometry modeling can be found in [57] and [66]. An interesting application of this concept to shell analysis is given in [52]. Another possibility for the analysis of domains described by their boundary is to resort to boundary related methods, where no volume mesh is required. The most developed method of this type is the Boundary Element Method (BEM), see *e.g.* [10]. In the direct BEM, the unknown boundary data are discretized, whereas in the indirect BEM, an auxiliary density function defined on the boundary is sought. This density function is used to describe the solution field. The indirect BEM can be seen as a Trefftz-type method. In such methods, the solution is approximated by a linear combination of basis functions, which fulfill the underlying partial differential equation. Reviews on Trefftz-type methods along with their classification can be found in [35] and [31]. A Trefftz-type which was developed with the aim to solve vibro-acoustic problems is the Wave Based Method (WBM) developed in [21]. Since its first publication, this method has been constantly developed further [18]. Within the WBM, the solution is determined by means of a variational formulation. Despite that the BEM would be optimal with respect to the model of the surrounding air, here, a more simpler approach, the MFS is used. This Trefftz-type method (see *e.g.* [24]) uses fundamental solutions of the underlying partial differential equation for the solution approximation. Typically, the solution is determined by collocation at the boundary. Due to the use of fundamental solutions, the Sommerfeld radiation condition is fulfilled exactly. Thus, unbounded domains are easily treatable. We mention three applications of the MFS in the field of poro-elasticity. Nennig *et al.*[45] applied the MFS to scattering problems from poro-elastic bodies in two dimensions. Wen and Liu [67] derived the fundamental solution for a poro-elastic plate in Laplace domain and applied the MFS for solving boundary value problems. Augustin

[5] presented density results and a MFS for quasi-static poro-elasticity.

In the present work, we couple the FEM and the MFS in order to benefit from both worlds. The coupling of different numerical methods is a well known approach for acoustic-structure interaction problems. The FEM is perfectly suited for models with complex geometries while boundary related methods enable to account for the radiation of waves in domains of infinite extent. The coupling of FEM-BEM is well-known in literature, see *e.g.* [25, 16, 69] among others for structural-acoustic coupling. The coupling of the FEM and the WBM has been proposed for different configurations. We mention the cases of structural (FEM) - acoustic fluid (WBM) coupling [65], acoustic fluid (WBM) - poroelastic domain (FEM) coupling [34] and the coupling of two different poroelastic domains [37]. For two-dimensional soil-structure interaction problems a coupled FEM-MFS schema has been developed in [30]. Thus, two elastic sub-domains are coupled. This was extended to a 2.5-dimensional model for the prediction of vibrations due to underground railway traffic in [3]. Furthermore, we mention [45], where an acoustic fluid domain is coupled with a poro-elastic domain. Both are discretized using the MFS. To our best knowledge, the coupling of a poro-elastic shell with an acoustic fluid was not considered before.

In the present work, the main novelty is the development of a layer-wise poro-elastic shell theory. The individual layer displacement kinematics are based on a seven-parameter shell model [4, 8, 17], whereas the scalar fluid pressure field is assumed to be quadratic through-the-thickness in each poro-elastic layer. The shell reference surface can be given either parametrically or implicitly. In both cases the exact geometry is incorporated in the FEM following the developments in [29]. The field approximation for the shell is done by means of arbitrary order hierarchical shape functions. Furthermore, a variational variant of the MFS in order to discretize the fluid domains is used. Schemata for the coupling of the FEM and the MFS at different interfaces are presented. Wile the coupling formulation at fluid - elastic solid interfaces are known in literature[65], to the best of our knowledge, the coupling formulation of a poro-elastic shell with a fluid is new. The implementation of the method is verified with high rigor. To that end, the method of manufactured solutions is adapted to the case of poro-elasticity for the first time. Finally, the proposed method is used to simulate the sound transmission from the inside of two cavities bounded by a poro-elastic shell structure to the infinite outer domain.

2 Governing equations

In this section the governing equations of an acoustic fluid, an elastic solid and a poro-elastic solid are briefly introduced. Harmonic time dependency of all fields is assumed where the angular frequency is denoted with ω.

2.1 Acoustic fluid

The propagation of sound waves in an fluid is governed by the Helmholtz equation [53]

$$k^2 p + \Delta p = g, \tag{1}$$

where p stands for the sound pressure fluctuation around the equilibrium state, $k = \omega\sqrt{\frac{\rho}{K}}$ is the wave number, g the source term, and Δ the Laplace operator. The material parameters are

the density ρ and the bulk modulus K. A pure acoustic boundary value problem equation (1) is supplemented by the boundary conditions

$$\begin{aligned} p(x,\omega) &= g_D(x,\omega) && \text{for } x \in \Gamma_D, \\ \frac{\partial_n p(x,\omega)}{\mathrm{i}\omega\rho} &= g_N(x,\omega) && \text{for } x \in \Gamma_N. \end{aligned} \tag{2}$$

On the Dirichlet boundary Γ_D, the pressure has the prescribed value g_D, whereas on the Neumann boundary Γ_N the normal velocity $\frac{\partial_n p(x,\omega)}{\mathrm{i}\omega\rho}$ has the prescribed value g_N. In the case of an unbounded domain, the solution has to fulfill the Sommerfeld radiation condition

$$\lim_{|x|\to\infty} |x| \left(\frac{\partial}{\partial |x|} + \mathrm{i}k \right) p(x) = 0, \tag{3}$$

first considered in [62].

2.2 Elastic solid

The propagation of waves in elastic solids is governed by the following equations

$$-\rho_s\, \omega^2 \mathbf{u} = \nabla \cdot \boldsymbol{\sigma} + \mathbf{b} \qquad \text{(balance of momentum)} \tag{4}$$

$$\boldsymbol{\sigma} = \mathbb{C} : \boldsymbol{\varepsilon} \qquad \text{(material law)} \tag{5}$$

$$\boldsymbol{\varepsilon} = \frac{1}{2}(\nabla \mathbf{u} + (\nabla \mathbf{u})^\top) \qquad \text{(kinematic relation).} \tag{6}$$

Here, $\mathbf{u}$ denotes the displacement vector, $\boldsymbol{\sigma}$ stands for the stress tensor, $\mathbf{b}$ is the volume load density, $\boldsymbol{\varepsilon}$ is the infinitesimal strain tensor, $\mathbb{C}$ denotes the fourth order elastic tensor, and ρ_s is the solid density. Here, we consider linear isotropic materials where the elasticity tensor is given by

$$\mathbb{C} = \frac{E\nu}{(1+\nu)(1-2\nu)}\, \mathbf{I} \otimes \mathbf{I} + \frac{E}{1+\nu}\, \mathsf{I} \tag{7}$$

where $\mathbf{I}$ is the second-rank identity tensor, and I is the symmetric part of the fourth-rank identity tensor. E denotes the Young's modulus and ν is the Poisson's ratio. The boundary conditions are given by

$$\begin{aligned} \mathbf{u}(x,\omega) &= \mathbf{u}^D(x,\omega) && \text{for } x \in \Gamma_D, \\ \mathbf{t}(x,\omega) &= \mathbf{t}^N(x,\omega) && \text{for } x \in \Gamma_N. \end{aligned} \tag{8}$$

On the Dirichlet boundary Γ_D the displacement vector has the prescribed value u^D. On the Neumann boundary Γ_N the surface traction vector has the prescribed value t_i^N.

2.3 Poro-elastic solid

Following Biot's theory, wave propagation in a poro-elastic solid is governed by the equations

$$\nabla \cdot \boldsymbol{\sigma}^{\mathrm{tot}} + \omega^2 \mathbf{u}\,(\rho + \rho_f \beta) - \beta\, \nabla p = 0, \tag{9a}$$

$$-\frac{\beta}{\omega^2 \rho_f} \Delta p + (\beta + \alpha)\, \nabla \cdot \mathbf{u} + \frac{\phi^2}{R} p = 0 \tag{9b}$$

Here, $\boldsymbol{\sigma}^{\text{tot}}$ stands for the total stress tensor

$$\boldsymbol{\sigma}^{\text{tot}} = \frac{E}{1+\nu}\,\boldsymbol{\varepsilon} + \frac{E\nu}{(1+\nu)(1-2\nu)}\,\text{tr}(\boldsymbol{\varepsilon})\,\mathbf{I} - \alpha p\,\mathbf{I}\,, \tag{10}$$

$\rho = (1-\phi)\rho_s + \phi\rho_f$ is the bulk density, ρ_f is the fluid density, ϕ denotes the porosity, R is a poro-elastic parameter, and α is the so-called effective stress coefficient [22]. To obtain (9) the relative fluid to solid displacement

$$\mathbf{U} - \mathbf{u} = \frac{\beta}{\omega^2\rho_f\phi}(-\nabla p + \omega^2\rho_f\mathbf{u}), \tag{11}$$

with the fluid displacement $\mathbf{U}$ has been eliminated. In (9) and (11) the abbreviation

$$\beta = \frac{\omega^2\rho_f\phi^2}{i\omega b - \omega^2(\phi\rho_f + \rho_a)}, \tag{12}$$

is used, where ρ_a is the apparent mass density and b is the viscous drag force.

For typical poro-elastic materials used in acoustic applications, the bulk modulus of the elastic solid K_s is very large as compared to the bulk modulus of the fluid K_f and the bulk modulus of the skeleton K. Thus, we assume an incompressible solid skeleton material which results in

$$\begin{aligned} R &= \phi K^f, \\ \alpha &= 1 \end{aligned} \tag{13}$$

Following [33], the frequency dependent viscous drag is given as

$$b(\omega) = \sigma\phi^2\sqrt{1 + \frac{4\mathrm{i}\,\alpha_\infty^2\,\eta_f\,\rho_f\,\omega}{\sigma^2\Lambda^2\phi^2}}\,. \tag{14}$$

Here, σ denotes the static flow resistivity and α_∞ is the tortuosity. Λ denotes the viscous characteristic length, and η_f is the dynamic viscosity. In order to take thermal effects into account, Champoux and Allard [14] introduced the thermal characteristic length Λ'. Following this approach, the bulk modulus of the fluid becomes frequency dependent

$$K^f(\omega) = \frac{\gamma\,p_0}{\gamma - \frac{\gamma-1}{\alpha'(\omega)}}. \tag{15}$$

Here, p_0 is the ambient pressure of air, γ is the ratio of specific heats and

$$\alpha'(\omega) = 1 + \frac{8\eta_f}{\mathrm{i}\omega\Lambda'^2 Pr\,\rho_f}\sqrt{1 + \mathrm{i}\rho_f\frac{Pr\Lambda'^2}{16\eta_f}}. \tag{16}$$

Here, Pr denotes the Prandtl number

$$Pr = \frac{c_p}{\eta_f\kappa}, \tag{17}$$

with the specific heat capacity at constant pressure c_p and the thermal conductivity κ.

The boundary conditions for a poro-elastic solid are given by

$$\begin{aligned} \mathbf{u}(x,\omega) &= \mathbf{u}^D(x,\omega) && \text{for } x \in \Gamma_D^u, \\ \mathbf{t}^{\text{tot}}(x,\omega) &= \mathbf{t}^N(x,\omega) && \text{for } x \in \Gamma_N^u, \\ p(x,\omega) &= p_D(x,\omega) && \text{for } x \in \Gamma_D^p, \\ q_n(x,\omega) &= q^N(x,\omega) && \text{for } x \in \Gamma_N^p. \end{aligned} \tag{18}$$

On the Dirichlet boundary for the solid Γ_D^u the displacement has a prescribed value $\mathbf{u}^D$, whereas on the Neumann boundary Γ_N^u the total surface traction vector is prescribed with $\mathbf{t}^N$. Furthermore, on the Dirichlet boundary for the fluid Γ_D^p the fluid pressure has a prescribed value p^D, whereas on the Neumann boundary Γ_N^p the normal flux

$$q_n = \frac{i\beta}{\omega\rho_f}\left(\omega^2\rho_f\mathbf{u} - \nabla p\right)\cdot\mathbf{n} \tag{19}$$

is prescribed with q^N. In general (Γ_D^u, Γ_N^u) and (Γ_D^p, Γ_N^p) can be two independent non-overlapping decompositions of the boundary. Thus, on a boundary point two conditions have to be fulfilled.

2.4 Coupling conditions

In this section, we outline the coupling conditions between the physical models. In Figure 2, the abstract setting of coupled continua is depicted. The domains Ω^a, Ω^e, Ω^p refer to an acoustic fluid, to an elastic solid and to a poro-elastic solid respectively. The boundary of Ω^a is denoted by $\Gamma^a = \Gamma_D^a \cup \Gamma_N^a \cup \Gamma^{ae} \cup \Gamma^{ap}$ and is the union of four non-overlapping parts. In view of all three models, Γ_D^o and Γ_N^o are the Dirichlet and the Neumann boundary of the domain Ω^o, $o \in \{a, e, p\}$. Γ^{ae} and Γ^{ap} denote the coupling boundary of the acoustic fluid domain Ω^a with the elastic solid domain Ω^e and the poro-elastic solid domain Ω^p. The boundary of Ω^e is denoted by $\Gamma^e = \Gamma_D^e \cup \Gamma_N^e \cup \Gamma^{ae} \cup \Gamma^{ep}$, whereas the boundary of Ω^p is $\Gamma^p = \Gamma_D^p \cup \Gamma_N^p \cup \Gamma^{ap} \cup \Gamma^{ep}$. The coupling boundary between Ω^e and Ω^p is Γ^{ep}. Before we consider the coupling of different models, we examine the coupling of two elastic continua. The coupling of two elastic continua (Ω_1, Ω_2) over the common interface Γ yields two conditions. The first condition which has to hold is the continuity of the displacements

$$\mathbf{u}^{(1)} = \mathbf{u}^{(2)} \quad \text{on } \Gamma. \tag{20}$$

The second condition is the equilibrium of forces, which results in

$$\mathbf{t}^{(1)} + \mathbf{t}^{(2)} = \mathbf{0} \quad \text{on } \Gamma. \tag{21}$$

In the case of an *acoustic fluid - elastic solid* interface Γ^{ae} also two coupling conditions are necessary. According to the inviscid assumption for the acoustic fluid, no shear stresses occur in the fluid. Hence, particles of the fluid can move tangential to the interface without resistance. Therefore, only the normal displacements are continuous

$$\mathbf{u}^a \cdot \mathbf{n} = \mathbf{u}^e \cdot \mathbf{n}. \tag{22}$$

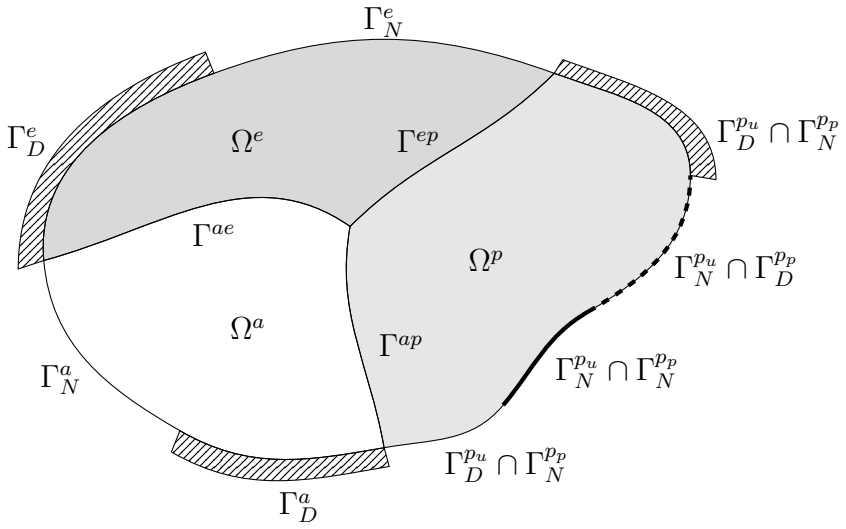

Figure 2: Coupled continua: acoustic fluid continuum Ω^a, elastic solid continuum Ω^e, poro-elastic solid continuum Ω^p

The fluid displacement can be expressed through the pressure by $\mathbf{u}^a = \frac{\rho^a}{\omega^2}\nabla p$. Thus, the coupling condition gets

$$\frac{\rho^a}{\omega^2}\nabla p^a \cdot \mathbf{n} = \mathbf{u}^e \cdot \mathbf{n} \quad \text{on } \Gamma^{ae}. \tag{23}$$

The traction on the interface resulting from the scalar pressure field in the fluid is $\mathbf{t}^a = -p^a\,\mathbf{n}$. Thus, the equilibrium of forces yields

$$\mathbf{t}^e = -p^a\,\mathbf{n} \quad \text{on } \Gamma^{ae}, \tag{24}$$

where the normal vector is the outward normal vector of the elastic domain.

On an *acoustic fluid - poro − elastic solid* interface Γ^{ap}, three coupling conditions have to be fulfilled. The continuity of normal displacements implies

$$\mathbf{u}^a \cdot \mathbf{n} = \mathbf{u}^p \cdot \mathbf{n} \quad \text{on } \Gamma^{ap}, \tag{25}$$

where $\mathbf{u}^p = (1-\phi)\mathbf{u} + \phi\mathbf{U}$ is the displacement of a 'poro-elastic particle'. Using the relative displacement between solid and fluid defined in (11), the coupling condition gets

$$\frac{\nabla p^a \cdot \mathbf{n}}{\rho^a \omega^2} = \mathbf{u} \cdot \mathbf{n} + \frac{1}{\mathrm{i}\omega}\mathbf{q} \cdot \mathbf{n} \quad \text{on } \Gamma^{ap}. \tag{26}$$

The second condition is given by the equilibrium of forces. The surface traction induced by the scalar pressure in the acoustic fluid has to be balanced with the total traction in the poro-elastic solid

$$-p^a\,\mathbf{n} = \mathbf{t}^{tot} \quad \text{on } \Gamma^{ap}, \tag{27}$$

where the normal vector is the outward normal vector of the poro-elastic domain. The third condition ensures the continuity of the pressure fields. Hence,

$$p^a = p^p \quad \text{on } \Gamma^{ap}. \tag{28}$$

The remaining combination is an *elastic solid - poro − elastic solid* interface Γ^{ep}. The elastic solid and the poro-elastic solid are able to resist shear forces. Therefore, no relative motion between the two solid phases are allowed

$$\mathbf{u}^s = \mathbf{u}^e \quad \text{on } \Gamma^{ep}. \tag{29}$$

The elastic domain represents an impervious interface for the fluid in the poro-elastic solid. Therefore, the relative mass flux normal to the interface has to be zero

$$\mathbf{q} \cdot \mathbf{n} = 0 \quad \text{on } \Gamma^{ep}. \tag{30}$$

As a third condition, the equilibrium of forces demands

$$\mathbf{t}^e + \mathbf{t}^{tot} = \mathbf{0} \quad \text{on } \Gamma^{ep}. \tag{31}$$

3 Poro-elastic shell structure

In this section, we describe a layer-wise theory for laminated poro-elastic shells. We consider shell reference surfaces $\bar{\Omega}$ which are given parametrically or implicitly. In the former case we have a parametrization $\overline{\mathfrak{g}} : \bar{U} \subset \mathbb{R}^2 \to \bar{\Omega}$ available with given parameter domain $\bar{U}$. In the latter case, the reference surface is given as the zero-level set of a function $\phi : \mathbb{R}^3 \to \mathbb{R}$ inside a cuboid B,

$$\bar{\Omega} = \{\mathbf{x} \in B | \, \phi(\mathbf{x}) = 0\}. \tag{32}$$

For this setting, the normal vector to the surface is given by

$$\tilde{\mathbf{n}}(\mathbf{x}) = \frac{\nabla \phi(\mathbf{x})}{||\nabla \phi(\mathbf{x})||}. \tag{33}$$

In the numerical method, we will make use of a piecewise parametrization of the exact surface over a space triangulation. Therefore, the implicit description of the reference surface is turned into a parametric one (cf. [27, 29]). Given the parametrization $\overline{\mathfrak{g}}$, we can define the two covariant base vectors $\overline{\mathbf{G}}_\alpha := \frac{\partial \overline{\mathfrak{g}}}{\partial \theta^\alpha}$, which span the tangent plane to $\bar{\Omega}$. Here and in the following, Greek indices take the values 1 and 2 and Latin indices the values 1, 2, 3. With the base vectors we can define the unit normal vector

$$\mathbf{n} = \frac{\overline{\mathbf{G}}_1 \times \overline{\mathbf{G}}_2}{||\overline{\mathbf{G}}_1 \times \overline{\mathbf{G}}_2||}. \tag{34}$$

Having defined the normal vector the parametrization of the three-dimensional shell volume Ω is given by

$$\begin{aligned} \mathfrak{g} : \; & (\bar{U} \times T) \subset \mathbb{R}^3 \to \Omega \subset \mathbb{R}^3 \\ & (\theta^1, \theta^2) \times \theta^3 \mapsto \mathfrak{g}(\theta^1, \theta^2, \theta^3) = \overline{\mathfrak{g}}(\theta^1, \theta^2) + \theta^3 \, \mathbf{n}, \end{aligned} \tag{35}$$

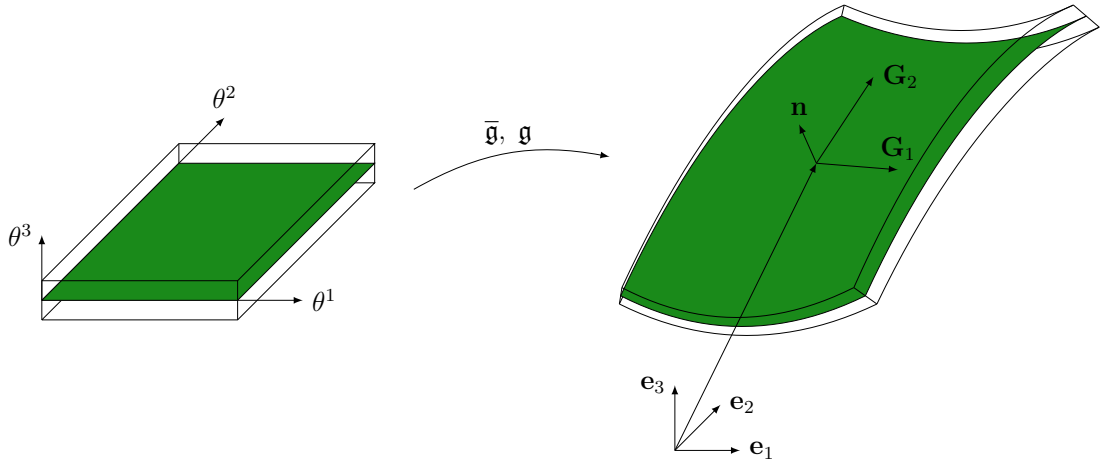

Figure 3: Parametrization of the shell. The parameter space on the left is mapped to the physical space on the right. The reference surface is parametrized by $\bar{\mathfrak{g}}$, whereas the shell volume is parametrized by $\mathfrak{g}$.

with the one-dimensional thickness interval T. The geometric setting is illustrated in Figure 3. We consider a layered shell structure with a layup as depicted in Figure 4. The total number of layers is L. Each layer has a thickness t_i, $i = 1 \dots L$ and is classified as elastic or poro-elastic. The distance from the reference surface to the bottom of the shell is denoted by t_0. Furthermore, we define the individual layer thickness intervals $T_i = \left[\sum_{j=0}^{i-1} t_j \, , \, \sum_{j=0}^{i} t_j\right]$. Thus, $T = \bigcup_{i=1}^{L} T_i$. The relations between the local thickness coordinate $\tau_i \in [0,1]$ of layer i and the global thickness coordinate $\theta^3 \in T_i$ are

$$\tau_i(\theta^3) = \frac{1}{t_i}\left(\theta^3 - \sum_{j=0}^{i-1} t_j\right), \tag{36}$$

and

$$\theta^3(\tau_i) = \sum_{j=0}^{i-1} t_j + t_i\,\tau_i\,. \tag{37}$$

The present layer-wise theory is based on the assumed seven-parameter displacement field for layer $\ell \in \{1,\dots,L\}$ of the form

$$\mathbf{u}^{\ell}(\theta^1,\theta^2,\theta^3) = \overset{(1)}{V}(\tau_\ell(\theta^3))\ \overset{(1,\ell)}{u_i}\ \mathbf{e}^i + \overset{(2)}{V}(\tau_\ell(\theta^3))\ \overset{(2,\ell)}{u_i}\ \mathbf{e}^i + \overset{(n)}{V}(\tau_\ell(\theta^3))\ \overset{(n,\ell)}{u}\ \mathbf{n}. \tag{38}$$

Here, $\overset{(\cdot)}{V}(\tau_\ell(\theta^3))$ are through-the-thickness functions and $\overset{(1,\ell)}{u}_i$, $\overset{2,\ell}{u}_i$, $\overset{(n,\ell)}{u}$ are seven local displacement parameters and $\mathbf{e}^i$ are the base vectors of a Cartesian coordinate system. The through-the-

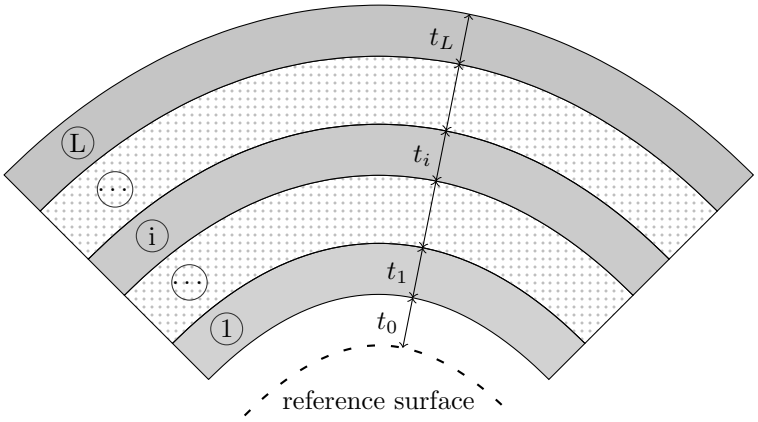

Figure 4: Layup of the shell

thickness functions are chosen as

$$\begin{aligned} \overset{(1)}{V}(\tau) &= 1-\tau, \\ \overset{(2)}{V}(\tau) &= \tau, \\ \overset{(n)}{V}(\tau) &= \tau^2-\tau. \end{aligned} \tag{39}$$

Thus, the parameters $\overset{(1,\ell)}{u_i} = \overset{(1,\ell)}{u_i}(\theta^1,\theta^2)$ and $\overset{(2,\ell)}{u_i} = \overset{(2,\ell)}{u_i}(\theta^1,\theta^2)$ describe the displacement of the bottom ($\tau=0$) and the top ($\tau=1$) of layer ℓ respectively. This is enhanced with the parameter $\overset{(n,\ell)}{u_i} = \overset{(n,\ell)}{u_i}(\theta^1,\theta^2)$, which accounts for a quadratic variation of the displacement in thickness direction, which vanishes at the bottom and the top surface of the layer. In all possible combinations of elastic and poro-elastic layers, the continuity of the displacement field is required. Thus, for two subsequent layers, we set

$$\overset{(2,\ell)}{u_i} = \overset{(1,\ell+1)}{u_i}. \tag{40}$$

Therefore, the total number of parameters describing the displacement is $3(L+1)+L$ and is independent of the stacking sequence. Following [60], the fluid pressure field in poro-elastic layers is approximated by a quadratic expansion through-the-thickness. The pressure field for layer ℓ is assumed to be of the form

$$p^\ell(\theta^1,\theta^2,\theta^3) = \overset{(1)}{V}(\tau_\ell(\theta^3))\overset{(1,\ell)}{p} + \overset{(2)}{V}(\tau_\ell(\theta^3))\overset{(2,\ell)}{p} + \overset{(n)}{V}(\tau_\ell(\theta^3))\overset{(n,\ell)}{p}, \tag{41}$$

where $\overset{(1,\ell)}{p} = \overset{(1,\ell)}{p}(\theta^1,\theta^2)$, $\overset{(2,\ell)}{p} = \overset{(2,\ell)}{p}(\theta^1,\theta^2)$, and $\overset{(n,\ell)}{p} = \overset{(n,\ell)}{p}(\theta^1,\theta^2)$ are three local parameters. Between two poro-elastic layers, we require the continuity of the pressure. Thus, if layer ℓ and $\ell+1$ both are poro-elastic, we set

$$\overset{(2,\ell)}{p} = \overset{(1,\ell+1)}{p}. \tag{42}$$

Therefore, the total number of parameters describing the fluid pressure is $3L_p - n_p$, where L_p is the number of poro-elastic layers and n_p is the number of interfaces between two poro-elastic

layers. Since the considered coupling of elastic and poro-elastic layers is natural [2], it is sufficient to enforce the continuity of the displacement field and the pressure field, as it is done in (40) and (42).

4 Numerical methods

4.1 Finite element method for the poro-elastic shell

The FEM developed for the layered poroelastic shell structure is based on the weak formulation of the respective governing equations (4) and (9) and on the through-the-thickness discretizations (38) and (41).

Weak form of elastodynamics The weak form of elastodynamics is obtained by multiplying (4) with a vector-valued test function $\bar{\mathbf{u}} \in V_0^u = \{\bar{\mathbf{u}} \in [H^1(\Omega)]^3 |\ \bar{\mathbf{u}} = 0 \text{ on } \Gamma_D\}$, integrating over the domain Ω and applying integration by parts we obtain

$$-\rho\ \omega^2 M_u(\mathbf{u},\bar{\mathbf{u}}) + K_u(\mathbf{u},\bar{\mathbf{u}}) = f_V(\bar{\mathbf{u}}) + f_N(\bar{\mathbf{u}}), \tag{43}$$

where

$$\begin{aligned} M_u(\mathbf{u},\bar{\mathbf{u}}) &= \int_\Omega \mathbf{u}\cdot\bar{\mathbf{u}}\ \mathrm{d}\mathbf{x}, \qquad & K_u(\mathbf{u},\bar{\mathbf{u}}) &= \int_\Omega (\mathbb{C} : \boldsymbol{\varepsilon}(\mathbf{u})) : \boldsymbol{\varepsilon}(\bar{\mathbf{u}})\ \mathrm{d}\mathbf{x}, \\ f_V(\bar{\mathbf{u}}) &= \int_\Omega \mathbf{b}\cdot\bar{\mathbf{u}}\ \mathrm{d}\mathbf{x}, \qquad & f_N(\bar{\mathbf{u}}) &= \int_{\Gamma_N} \mathbf{t}^N\ \bar{\mathbf{u}}\ \mathrm{d}s_x. \end{aligned} \tag{44}$$

Thus, the weak form of the problem reads: Find $\mathbf{u} \in V^u = \{\mathbf{u} \in [H^1(\Omega)]^3 |\ \mathbf{u} = \mathbf{u}^D \text{ on } \Gamma_D^u\}$ such that (43) is fulfilled for all $\bar{\mathbf{u}} \in V_0$.

Weak form of poro-elasticity The derivation of the weak form of poro-elasticity follows the same arguments as for elastodynamics. We multiply (9a) with vector-valued test function $\bar{\mathbf{u}} \in V_0^u$, integration over the domain and apply integration by parts,

$$-\int_\Omega \boldsymbol{\sigma}^{\mathrm{tot}} : \nabla\bar{\mathbf{u}}\ \mathrm{d}\mathbf{x} + \int_\Gamma \mathbf{t}^{\mathrm{tot}}\cdot\bar{\mathbf{u}}\ \mathrm{d}s_{\mathbf{x}} + \int_\Omega \left(\omega^2\mathbf{u}\,(\rho+\rho_f\beta) - \beta\nabla p\right)\cdot\bar{\mathbf{u}}\ \mathrm{d}\mathbf{x} = 0. \tag{45}$$

Furthermore, we multiply (9b) with a scalar test function $\bar{p} \in V_0^p = \{\bar{p} \in H^1(\Omega) |\ \bar{p} = 0 \text{ on } \Gamma_D^p\}$ and perform an integration over the domain. This yields with some rearrangements

$$\int_\Omega \frac{\beta}{\omega^2\rho_f}\nabla\cdot(\omega^2\rho_f\mathbf{u} - \nabla p)\bar{p}\ \mathrm{d}\mathbf{x} + \int_\Omega \nabla\cdot\mathbf{u}\ \bar{p}\ \mathrm{d}\mathbf{x} + \frac{\phi^2}{R}\int_\Omega p\,\bar{p}\ \mathrm{d}\mathbf{x} = 0. \tag{46}$$

Now, we apply integration by parts to the first integral and using (19) in order to obtain

$$-\int_\Omega \frac{\beta}{\omega^2\rho_f}(\omega^2\rho_f\mathbf{u} - \nabla p)\nabla\bar{p}\ \mathrm{d}\mathbf{x} + \int_{\Gamma_N^p} \frac{q_N\,\bar{p}}{i\omega}\mathrm{d}s_x + \int_\Omega \nabla\cdot\mathbf{u}\ \bar{p}\ \mathrm{d}\mathbf{x} + \frac{\phi^2}{R}\int_\Omega p\,\bar{p}\ \mathrm{d}\mathbf{x} = 0. \tag{47}$$

Thus, we can formulate the weak form of the poroelastic boundary value problem: Find $(\mathbf{u}, p) \in V^u \times V^p$ such that

$$\begin{aligned} -K_u(\mathbf{u},\bar{\mathbf{u}}) + \omega^2 \left(\rho + \beta\rho^f\right) M_u(\mathbf{u},\bar{\mathbf{u}}) + D(p,\bar{\mathbf{u}}) - L(p,\bar{\mathbf{u}}) + f_u(\bar{\mathbf{u}}) = 0, \\ K_p(p,\bar{p}) + M_p(p,\bar{p}) + D(\bar{p},\mathbf{u}) - L(\bar{p},\mathbf{u}) + f_p(\bar{p}) = 0, \end{aligned} \tag{48}$$

are fulfilled for all test functions $(\bar{\mathbf{u}}, \bar{p}) \in V_0^u \times V_0^p$. The bilinear and linear forms in (48) are defined in (44) and

$$\begin{aligned} K_p(p,\bar{p}) &= \frac{\beta}{\omega^2\rho^f} \int_\Omega \nabla p \cdot \nabla \bar{p} \ \mathrm{d}\mathbf{x}, & M_p(p,\bar{p}) &= \frac{\phi^2}{R} \int_\Omega p\ \bar{p} \ \mathrm{d}\mathbf{x}, \\ D(p,\bar{\mathbf{u}}) &= \int_\Omega p\, \nabla\cdot\bar{\mathbf{u}} \ \mathrm{d}\mathbf{x}, & L(p,\bar{\mathbf{u}}) &= \beta \int_\Omega \nabla p \cdot \bar{\mathbf{u}} \ \mathrm{d}\mathbf{x}, \\ f_u(\bar{\mathbf{u}}) &= \int_{\Gamma_N^u} \mathbf{t}^N \bar{\mathbf{u}} \, \mathrm{d}s_{\mathbf{x}}, & f_p(\bar{p}) &= \int_{\Gamma_N^p} \frac{q_N\, \bar{p}}{i\omega} \, \mathrm{d}s_{\mathbf{x}}. \end{aligned} \tag{49}$$

Discretization The discretization is based on the standard reference element technique, *i.e.* on the reference element hierarchical shape functions of arbitrary order and quadrature are defined [61]. Thus, the shell reference surface is subdivided into n_e non-overlapping geometric elements τ_e such that $\bar{\Omega} = \bigcup_{e=1}^{n_e} \tau_e$. In the case of an parametrically defined reference surface the parametric domain is subdivided into quadrilaterals Q_e and the geometric elements in real space are given by $\tau_e = \overline{\mathfrak{g}}(Q_e)$, see Figure 5. The standard affine mapping from the reference element τ_R to Q_e is denoted by Φ^e. For implicitly defined reference surfaces the parametrization $\overline{\mathfrak{g}}$ is not explicitly available. Therefore, the exact geometry is parametrized over a piecewise flat triangulation with elements ψ_e in real space, see Figure 6. The elements in real space are obtained by $\tau_e = a_e(\psi_e)$. Here, a_e is a mapping which is only implicitly defined [27, 29], *i.e.* for the evaluation a one-dimensional nonlinear root finding problem has to be solved. For further details on the evaluation of the integrals in (44) and (49) we refer to [28].

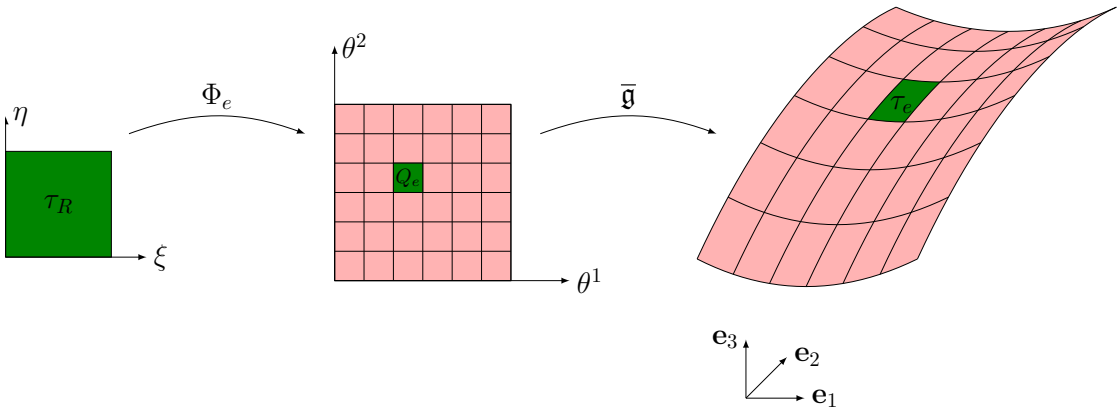

Figure 5: Geometry mappings for parametrically given shells

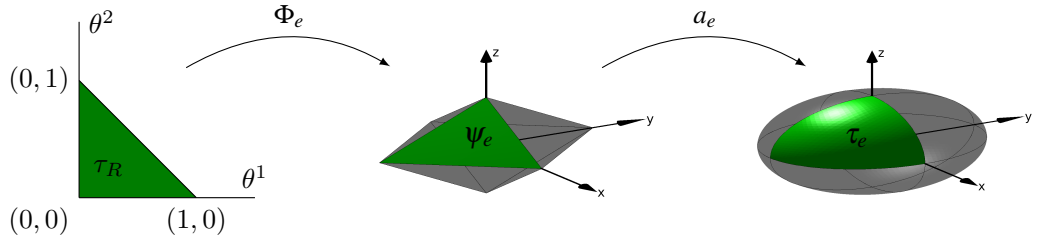

Figure 6: Geometry mappings for implicitly given shells

4.2 Method of fundamental solutions for a single fluid domain

In this section, we will introduce a variant of the MFS, which is a Trefftz-type method. This method is used to discretize the acoustic fluid surrounding the shell structure. In general, a Trefftz method consists of a discrete Trefftz space and a Trefftz variational formulation [31]. Usually, the MFS refers to a particular combination of discrete space and variational formulation. The ansatz functions are fundamental solutions (Green's function) with source points placed along a curve (in 2D) or on a surface (in 3D) surrounding the computational domain Ω. It is necessary that the source points lie in the complement of Ω, since the fundamental solutions are singular at the source points. The coefficients are determined by collocation. Here, we want to solve the boundary value problem of acoustics (2). The well known fundamental solution of the Helmholtz operator in the full 3D space is given by

$$\mathscr{G}^{3D}(\mathbf{x},\mathbf{y}) = \frac{\mathrm{e}^{-\mathrm{i}kr}}{4\pi r}, \quad r = ||\mathbf{y}-\mathbf{x}||. \tag{50}$$

The point $\mathbf{x}$ is called field point, whereas $\mathbf{y}$ is called source point. We restrict our further considerations to half-space problems. This means that we assume that the upper half-space $\Omega_+ = \{(x,y,z) \in \mathbb{R}^3 | z > 0\}$ is divided by the shell structure Ω^s into two fluid domains Ω^{int} and Ω^{ext}, such that $\Omega_+ = \Omega^{int} \cup \Omega^{ext} \cup \Omega^s$. We assume a sound hard surface $\partial\Omega_+$ at $z = 0$. Thus, the normal fluid velocity vanishes,

$$\mathbf{v}^a(\mathbf{x}) \cdot \mathbf{e}_3 = 0, \quad \text{for } \mathbf{x} \in \partial\Omega_+. \tag{51}$$

By making use of the well known half-space fundamental solution, the condition at sound hard surface $\partial\Omega_+$ is fulfilled exactly. The half-space fundamental solution is given by[9]

$$\mathscr{G}(\mathbf{x},\mathbf{y}) = \frac{\mathrm{e}^{-\mathrm{i}kr}}{4\pi r} + \frac{\mathrm{e}^{-\mathrm{i}k\tilde{r}}}{4\pi\tilde{r}}, \quad \tilde{r} = ||\tilde{\mathbf{y}}-\mathbf{x}||, \quad \tilde{\mathbf{y}} = (y_1, y_2, -y_3). \tag{52}$$

In the present work, we use fundamental solutions placed on a surface embracing the fluid domain to approximate the pressure field in the acoustic fluid, as it is done in the classical MFS. The unknown coefficients are determined by a variational formulation, like in the WBM [18]. To this end, the residuals

$$\begin{aligned} R_D(x) &= p(x) - g_D(x) && \text{for } x \in \Gamma_D, \\ R_N(x) &= \frac{\nabla p(x) \cdot \mathbf{n}(x)}{\mathrm{i}\omega\rho} - g_N(x) && \text{for } x \in \Gamma_N, \end{aligned} \tag{53}$$

are introduced. The solution in the fluid domain is approximated by a linear combination of fundamental solutions $\mathscr{G}$ weighted with coefficients c_i

$$p^a(\mathbf{x}) = \sum_{i=1}^{N_p} c_i \, \mathscr{G}(\mathbf{x}, \mathbf{y}_i). \tag{54}$$

In order to treat non-homogeneous problems, *i.e.* where sources are located inside the acoustic fluid domain, we extend (54) to

$$p^a = \sum_{i=1}^{N_s} c_i \, \mathscr{G}(\mathbf{x}, \mathbf{y}_i) + F_p, \tag{55}$$

where F_p are particular solutions of the in-homogeneous problem. In the present work, we consider point sources only. Thus, F_p is a linear combination of fundamental solutions

$$F_p = \sum_{s=1}^{N_p} d_s \, \mathscr{G}(\mathbf{x}, \mathbf{y}_s), \tag{56}$$

where d_s is the strength of an acoustic source at $\mathbf{y}_s$. The discrete fluid displacement is given by

$$\mathbf{u}^a(\mathbf{x}) = \frac{1}{\rho^a \omega^2} \sum_{i=1}^{N_p} c_i \mathscr{H}(\mathbf{x}, \mathbf{y}_i). \tag{57}$$

where

$$\mathscr{H}(\mathbf{x}, \mathbf{y}) = \nabla_{\mathbf{x}} \mathscr{G}(\mathbf{x}, \mathbf{y}). \tag{58}$$

Thus,

$$\mathscr{H}(\mathbf{x}, \mathbf{y}) \cdot \mathbf{e}_j = (1 + \mathrm{i}kr) \frac{y_j - x_j}{4\pi r^3} \, \mathrm{e}^{-\mathrm{i}kr} + (1 + \mathrm{i}k\tilde{r}) \frac{\tilde{y}_j - x_j}{4\pi \tilde{r}^3} \, \mathrm{e}^{-\mathrm{i}k\tilde{r}}. \tag{59}$$

In the proposed MFS either the interior acoustic problem in Ω^{int} or the exterior acoustic problem Ω^{ext} can be tackled. In both cases, we assume that the boundary Γ of the respective domain can be decomposed into $\Gamma = \Gamma_D \cup \Gamma_N \cup \partial\Omega_+$. Due to the ansatz (55), the Helmholtz equation in Ω_+ and the hard wall condition at $\partial\Omega_+$ are fulfilled exactly. Nevertheless, the other boundary conditions cannot be fulfilled exactly, yielding the residua (53). Therefore, the unknown coefficients c_i in (55) are determined in a weighted residual sense. To this end, the boundary residua are weighted with the complex conjugate of the test functions η and their normal derivative,

$$\int_{\Gamma_D} \frac{\nabla \bar{\eta}(x) \cdot \mathbf{n}(x)}{\mathrm{i}\omega\rho} R_D(x) \, \mathrm{d}s_{\mathbf{x}} + \int_{\Gamma_N} \bar{\eta}(x) R_N(x) \, \mathrm{d}s_{\mathbf{x}} = 0. \tag{60}$$

Applying a Galerkin approach, the test functions $\bar{\eta}$ are chosen to be fundamental solutions with the same source points as in (54). This leads to the linear system of equations

$$K^{\mathrm{MFS}} u^{\mathrm{MFS}} = f^{\mathrm{MFS}}, \tag{61}$$

where matrix and vector entries are given by

$$
\begin{aligned}
K^{\mathrm{MFS}}[i,j] &= \int_{\Gamma_D} \mathscr{H}(\mathbf{x},\mathbf{y}_i)\cdot\mathbf{n}(\mathbf{x})\,\mathscr{G}(\mathbf{x},\mathbf{y}_j)\,\mathrm{d}s_{\mathbf{x}} \\
&\quad + \int_{\Gamma_N} \mathscr{G}(\mathbf{x},\mathbf{y}_i)\,\mathscr{H}(\mathbf{x},\mathbf{y}_j)\cdot\mathbf{n}(\mathbf{x})\,\mathrm{d}s_{\mathbf{x}}, \\
u^{\mathrm{MFS}}[i] &= c_i, \\
f^{\mathrm{MFS}}[i] &= \int_{\Gamma_D} \mathscr{H}(\mathbf{x},\mathbf{y}_i)\cdot\mathbf{n}(\mathbf{x})\,\left(g_D - \sum_{l=1}^{N_p} d_l \mathscr{G}(\mathbf{x},\mathbf{y}_l)\right)\,\mathrm{d}s_{\mathbf{x}} \\
&\quad + \int_{\Gamma_N} \mathscr{G}(\mathbf{x},\mathbf{y}_i)\,\left(g_N - \sum_{l=1}^{N_p} d_l \mathscr{H}(\mathbf{x},\mathbf{y}_l)\cdot\mathbf{n}(\mathbf{x})\right)\,\mathrm{d}s_{\mathbf{x}}.
\end{aligned}
\tag{62}
$$

4.3 Coupled method

In this section we present a coupling approach for the FEM and the MFS.

Acoustic-elastic FEM-MFS coupling We consider the case of an elastic solid which is in contact with an acoustic fluid at the interface Γ^{ae}. The presented formulation is similar to the one in [65]. The variational formulation of the governing equations for an elastic solid is rewritten to

$$
-\rho\ \omega^2 M_u(\mathbf{u}^e,\bar{\mathbf{u}}) + K_u(\mathbf{u}^e,\bar{\mathbf{u}}) - \int_{\Gamma^{ae}} \mathbf{t}^e\cdot\bar{\mathbf{u}}\,\mathrm{d}s_{\mathbf{x}} = f_V(\bar{\mathbf{u}}) + f_N(\bar{\mathbf{u}}). \tag{63}
$$

Here, we have assumed the case $\Gamma = \Gamma_N \cup \Gamma_D \cup \Gamma^{ae}$. The case of an additional interface between an elastic solid and a poro-elastic solid was commented in Section 3. The two coupling conditions for the interface Γ^{ae} stated in (23) and (24) are rewritten to

$$
\mathbf{t}^e = -p^a\,\mathbf{n}, \quad \text{on } \Gamma^{ae}, \tag{64}
$$

and

$$
\frac{1}{\rho^a\omega^2}\nabla p\cdot\mathbf{n} - \mathbf{u}^e\cdot\mathbf{n} = 0, \quad \text{on } \Gamma^{ae}. \tag{65}
$$

The incorporation of the first coupling condition in (63) yields

$$
-\rho\ \omega^2 M_u(\mathbf{u}^e,\bar{\mathbf{u}}) + K_u(\mathbf{u}^e,\bar{\mathbf{u}}) + \int_{\Gamma^{ae}} p^a\,\mathbf{n}\cdot\bar{\mathbf{u}}\,\mathrm{d}s_{\mathbf{x}} = f_V(\bar{\mathbf{u}}) + f_N(\bar{\mathbf{u}}). \tag{66}
$$

Following the variational MFS approach in Section 4.2, the second coupling condition is weighted with the complex conjugate of the test function η and integrated over the coupling interface

$$
\int_{\Gamma^{ae}} \bar{\eta}(x)\left(\frac{1}{\rho^a\omega^2}\nabla p\cdot\mathbf{n} - \mathbf{u}^e\cdot\mathbf{n}\right)\,\mathrm{d}s_{\mathbf{x}}. \tag{67}
$$

The discretization of (65) and (67) leads to a system of equations in the form of

$$\begin{bmatrix} -\omega^2 M_u + K_u & G_1 \\ (G_1)^\top & -H \end{bmatrix} \begin{bmatrix} u_i \\ c_k \end{bmatrix} = \begin{bmatrix} f_V + f_N - f_{ae} \\ f_p \end{bmatrix}. \tag{68}$$

The matrices M_u and K_u are the mass and the stiffness matrix and $f_V + f_N$ is the load vector, which arise from the FEM discretization. In order to state the entries of the other matrices, we use the global index $i = i(i_1, i_2, i_3, l)$, which refers to the respective finite element function $N_{i_1}(\mathbf{x}) \overset{(i_3)}{V}(\tilde{\boldsymbol{\tau}}^l(\mathbf{x})) \overset{(i_3,l)}{u_{i_2}} \mathbf{e}_{i_2}$. Here, N_{i_1} denotes a two-dimensional finite element shape function. Thus,

$$\begin{aligned} G_1[i,k] &= \int_{\Gamma^{ae}} N_{i_1}(\mathbf{x}) \overset{(i_3)}{V}(\tilde{\boldsymbol{\tau}}^l(\mathbf{x}))\, \mathscr{G}(\mathbf{x}, \mathbf{y}_k)\, \mathbf{e}_{i_2} \cdot \mathbf{n}^e(\mathbf{x})\, \mathrm{d}s_x, \\ H[k,l] &= \frac{1}{\rho^a \omega^2} \int_{\Gamma^{ae}} \mathscr{H}(\mathbf{x}, \mathbf{y}_l) \cdot \mathbf{n}(\mathbf{x})\, \mathscr{G}(\mathbf{x}, \mathbf{y}_k)\, \mathrm{d}s_x, \\ f_{ae}[i] &= \sum_{s=1}^{N_s} d_s \int_{\Gamma^{ae}} N_{i_1}(\mathbf{x})\, \mathscr{G}(\mathbf{x}, \mathbf{y}_s)\, \mathbf{e}_{i_2} \cdot \mathbf{n}^e(\mathbf{x})\, \mathrm{d}s_{\mathbf{x}}, \\ f_p[k] &= \sum_{s=1}^{N_s} \frac{d_s}{\rho^a \omega^2} \int_{\Gamma^{ae}} \mathscr{H}(\mathbf{x}, \mathbf{y}_s) \cdot \mathbf{n}(\mathbf{x})\, \mathscr{G}(\mathbf{x}, \mathbf{y}_k)\, \mathrm{d}s_{\mathbf{x}}. \end{aligned} \tag{69}$$

Using $\Delta \mathscr{G}(\mathbf{x}, \mathbf{y}) = 0$, $\forall \mathbf{x} \neq \mathbf{y}$ and applying integration by parts two times,

$$\begin{aligned} 0 &= \int_\Omega \Delta \mathscr{G}(\mathbf{x}, \mathbf{y}_i) \mathscr{G}(\mathbf{x}, \mathbf{y}_j)\, \mathrm{d}\mathbf{x} \\ &= \int_\Gamma \mathscr{H}(\mathbf{x}, \mathbf{y}_i) \cdot \mathbf{n}(\mathbf{x}) \mathscr{G}(\mathbf{x}, \mathbf{y}_j)\, \mathrm{d}s_{\mathbf{x}} - \int_\Omega \nabla \mathscr{G}(\mathbf{x}, \mathbf{y}_i) \cdot \nabla \mathscr{G}(\mathbf{x}, \mathbf{y}_j)\, \mathrm{d}\mathbf{x} \\ &= \int_\Gamma \mathscr{H}(\mathbf{x}, \mathbf{y}_i) \cdot \mathbf{n}(\mathbf{x}) \mathscr{G}(\mathbf{x}, \mathbf{y}_j)\, \mathrm{d}s_{\mathbf{x}} - \int_\Gamma \mathscr{G}(\mathbf{x}, \mathbf{y}_i) \mathscr{H}(\mathbf{x}, \mathbf{y}_j) \cdot \mathbf{n}(\mathbf{x})\, \mathrm{d}s_{\mathbf{x}} + \int_\Omega \mathscr{G}(\mathbf{x}, \mathbf{y}_i) \Delta \mathscr{G}(\mathbf{x}, \mathbf{y}_j)\, \mathrm{d}\mathbf{x} \\ &= \int_\Gamma \mathscr{H}(\mathbf{x}, \mathbf{y}_i) \cdot \mathbf{n}(\mathbf{x}) \mathscr{G}(\mathbf{x}, \mathbf{y}_j)\, \mathrm{d}s_{\mathbf{x}} - \int_\Gamma \mathscr{G}(\mathbf{x}, \mathbf{y}_i) \mathscr{H}(\mathbf{x}, \mathbf{y}_j) \cdot \mathbf{n}(\mathbf{x})\, \mathrm{d}s_{\mathbf{x}}, \end{aligned} \tag{70}$$

yields

$$\int_\Gamma \mathscr{H}(\mathbf{x}, \mathbf{y}_i) \cdot \mathbf{n}(\mathbf{x}) \mathscr{G}(\mathbf{x}, \mathbf{y}_j)\, \mathrm{d}s_{\mathbf{x}} = \int_\Gamma \mathscr{G}(\mathbf{x}, \mathbf{y}_i) \mathscr{H}(\mathbf{x}, \mathbf{y}_j) \cdot \mathbf{n}(\mathbf{x})\, \mathrm{d}s_{\mathbf{x}}, \tag{71}$$

and we obtain that the matrix H is symmetric. Therefore, the system matrix of (68) is symmetric. We remark that the integrals are transformed to the reference element for their numerical evaluation by means of a quadrature rule.

Acoustic−poro-elastic FEM-MFS coupling. We proceed with the coupling in the case of an acoustic fluid where the pressure field is approximated by an MFS ansatz and a poroelastic solid, which is discretized by the FEM. Our formulation is different to the one in [34], with the feature

of yielding a symmetric system matrix. We rewrite the variational formulation of the governing equations for a poroelastic solid stated in (48) to

$$\begin{aligned} -K_u(\mathbf{u},\bar{\mathbf{u}}) + \tilde{M}_u(\mathbf{u},\bar{\mathbf{u}}) + D(p,\bar{\mathbf{u}}) - L(p,\bar{\mathbf{u}}) + f_u(\bar{\mathbf{u}}) - \int\limits_{\Gamma^{ap}} \mathbf{t}^{\text{tot}} \cdot \bar{\mathbf{u}} \, \mathrm{d}s_{\mathbf{x}} = 0, \\ K_p(p,\bar{p}) + M_p(p,\bar{p}) + D(\bar{p},\mathbf{u}) - L(\bar{p},\mathbf{u}) + f_p(\bar{p}) + \int\limits_{\Gamma^{ap}} \frac{\mathbf{q}\cdot\mathbf{n}^p}{i\omega} \bar{p} \; \mathrm{d}s_{\mathbf{x}} = 0, \end{aligned} \tag{72}$$

with $\tilde{M}_u(\mathbf{u},\bar{\mathbf{u}}) = \omega^2 \left(\rho + \beta\rho^f\right) M_u(\mathbf{u},\bar{\mathbf{u}})$. Here, we have assumed that $\Gamma = \Gamma_N \cup \Gamma_D \cup \Gamma^{ap}$. We incorporate the coupling condition (27) and (28) in the first equation of (72), which gives for the integral over Γ^{ap}

$$-\int\limits_{\Gamma^{ap}} \mathbf{t}^{\text{tot}} \cdot \bar{\mathbf{u}} \, \mathrm{d}s_{\mathbf{x}} = \int\limits_{\Gamma^{ap}} p\,\mathbf{n} \cdot \bar{\mathbf{u}} \, \mathrm{d}s_{\mathbf{x}}. \tag{73}$$

The coupling condition (26) is incorporated in the second equation of (72). For the integral over Γ^{ap}, we obtain

$$\int\limits_{\Gamma^{ap}} \frac{\mathbf{q}\cdot\mathbf{n}}{i\omega} \bar{p} \; \mathrm{d}s_{\mathbf{x}} = \int\limits_{\Gamma^{ap}} \left(\frac{\nabla p^a \cdot \mathbf{n}}{\rho^a \omega^2} - \mathbf{u}\cdot\mathbf{n} \right) \bar{p} \; \mathrm{d}s_{\mathbf{x}}. \tag{74}$$

Following the variational MFS approach in Section 4.2, the coupling condition (28) is weighted with the gradient of the complex conjugate of the test function η and integrated over the coupling interface

$$\int\limits_{\Gamma^{ae}} \nabla\bar{\eta}(x) \cdot \mathbf{n} \, (p^a - p) \; \mathrm{d}s_{\mathbf{x}} = 0. \tag{75}$$

After discretization we have the symmetric system of equations

$$\begin{bmatrix} K_u - \tilde{M}_u & L - D - M_\Gamma & 0 \\ (L)^\top - (D)^\top - (M_\Gamma)^\top & K_p + M_p & G_2 \\ 0 & (G_2)^\top & -H \end{bmatrix} \begin{bmatrix} u_i \\ p_j \\ c_k \end{bmatrix} = \begin{bmatrix} f_N^u - f_{ap}^u \\ -f_{N_p} - f_{ap}^p \\ f_{p_2} \end{bmatrix}, \tag{76}$$

where the newly introduced matrices and vectors are

$$\begin{aligned} G_2[j,k] &= \int\limits_{\Gamma^{ap}} N_{j_1}(\mathbf{x}) \overset{(j_2)}{V}(\tilde{\boldsymbol{\tau}}^l(\mathbf{x})) \, \mathscr{H}(\mathbf{x},\mathbf{y}_k) \cdot \mathbf{n}(\mathbf{x}) \, \mathrm{d}s_x, \\ M_\Gamma[i,j] &= \int\limits_{\Gamma^{ap}} N_{j_1}(\mathbf{x}) \overset{(j_2)}{V}(\tilde{\boldsymbol{\tau}}^l(\mathbf{x})) N_{i_1}(\mathbf{x}) \overset{(i_3)}{V}(\tilde{\boldsymbol{\tau}}^l(\mathbf{x})) \, \mathbf{e}_{i_2} \cdot \mathbf{n}(\mathbf{x}) \, \mathrm{d}s_x, \\ f_{ap}^u[i] &= \sum_{s=1}^{N_s} d_s \int\limits_{\Gamma^{ap}} N_{i_1}(\mathbf{x}) \overset{(i_3)}{V}(\tilde{\boldsymbol{\tau}}^l(\mathbf{x})) \, \mathscr{G}(\mathbf{x},\mathbf{y}_s) \, \mathbf{e}_{i_2} \cdot \mathbf{n}^e(\mathbf{x}) \, \mathrm{d}s_{\mathbf{x}}, \\ f_{ap}^p[j] &= \sum_{s=1}^{N_s} d_s \int\limits_{\Gamma^{ap}} N_{j_1}(\mathbf{x}) \overset{(j_2)}{V}(\tilde{\boldsymbol{\tau}}^l(\mathbf{x})) \, \mathscr{H}(\mathbf{x},\mathbf{y}_s) \cdot \mathbf{n}^e(\mathbf{x}) \, \mathrm{d}s_{\mathbf{x}}, \\ f_{p_2}[k] &= \sum_{s=1}^{N_s} \frac{d_s}{\rho^a \omega^2} \int\limits_{\Gamma^{ap}} \mathscr{G}(\mathbf{x},\mathbf{y}_s) \, \bar{\mathscr{H}}(\mathbf{x},\mathbf{y}_k) \cdot \mathbf{n}(\mathbf{x}) \, \mathrm{d}s_{\mathbf{x}}. \end{aligned} \tag{77}$$

5 Numerical results

5.1 Verification

The aim of this section is to verify the implementation of the methods developed in Section 4. In order to ensure the reliability of a numerical simulation software, verification and validation ($V\&V$) are unavoidable tasks [46, 47].

5.1.1 Verification of the poro-elastic shell FEM

In this section, we apply code verification to the poro-elastic shell FEM developed in Section 4.1 based on order-of-accuracy tests and on the method of manufactured solutions (MMS) [59, 54, 56, 38, 26]. The necessary prerequisite to apply an order-of-accuracy test to a numerical schema is the knowledge of a formal order of convergence and exact solutions. Thus, one has to know an estimate of the type

$$||u^{exact} - u^{numerical}|| \leq C h^q \, ||u^{exact}||, \tag{78}$$

where C is a constant and h is a characteristic discretization parameter. Here, we refer to a characteristic element size. Then q is called the formal order of convergence with respect to the norm $||\cdot||$. For two meshes with characteristic element sizes h_1 and h_2, the experimental order of convergence (eoc) is defined as

$$eoc = \frac{\log(e_1) - \log(e_2)}{\log(h_1) - \log(h_2)}, \tag{79}$$

where

$$e_i = ||u^{exact} - u^{numerical}_{h_i}|| \tag{80}$$

is the numerical error corresponding to the discretization h_i. The code is verified, if the eoc matches the formal order of convergence within the asymptotic range. For the FEM with arbitrary ansatz order p applied here, we expect $q = p+1$ for the error in the L_2 norm for smooth solutions.

In the case of the elastic solid problem (8), the procedure above is straightforwardly applicable. The implemented finite element code needs the components b^i of the source term $\mathbf{b} = b^i \mathbf{e}_i$ with respect to the global Cartesian frame. In the case of the poro-elastic solid problem (9), we include artificial source terms in the formulation, in order to apply the MMS. We modify the respective equations (9) to

$$\begin{aligned} \mathbf{b}^u &= \nabla \cdot \boldsymbol{\sigma}^{\mathrm{tot}} + \omega^2 \mathbf{u} \, (\rho + \rho_f \beta) - \beta \, \nabla p, \\ b^p &= -\frac{\beta}{\omega^2 \rho_f} \Delta p + (\beta + \alpha) \, \nabla \cdot \mathbf{u} + \frac{\phi^2}{R} p. \end{aligned} \tag{81}$$

We remark that these source terms have no physical meaning. They are incorporated in the variational formulation and in the FEM easily, leading to additional entries in the load vectors.

	Example 1	Example 2	Example 3
$\overset{(1)}{u_i^M}$	$[0 \quad 0 \quad 0]$	$[\cos(20\theta^1) \quad 0 \quad 0]$	$[xy \quad 0 \quad 0]$
$\overset{(2)}{u_i^M}$	$[0 \quad 0 \quad 0]$	$[\cos(20\theta^1) \quad 0 \quad 0]$	$[x \quad 0 \quad 0]$
$\overset{(n)}{u^M}$	0	$\exp(\theta^2)$	z
$\overset{(1)}{p^M}$	$\exp(\theta^1)\sin(20\theta^2)$	0	z
$\overset{(2)}{p^M}$	$\exp(\theta^2)\sin(\theta^1)$	0	0
$\overset{(n)}{p^M}$	$\cos(\theta^1)\sin(\theta^2)$	0	0

Table 1: Parameters for the manufactured solutions

Verification examples We have checked the order of convergence for a number of examples, considering different material parameters, frequencies, geometries, displacement fields, and pressure fields. In all examples, the optimal asymptotic order of convergence could be observed.

In this section, we show the results of four verification examples in total. In the first three examples, we use a parametric description of the reference surface, whereas in the fourth example, an implicit description is used. In the first example, we prescribe the trivial displacement solution and a non-trivial pressure solution. In the second example, we make it the other way round. In both examples, we use the reference surface given by

$$\begin{aligned} x &= \theta^1, \\ y &= \theta^2, \\ z &= \theta^1\,\theta^2 \end{aligned} \tag{82}$$

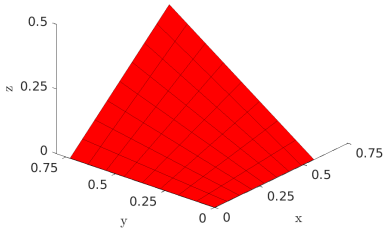

and $\theta^1 \in [0, 0.56]$ and $\theta^2 \in [0, 0.73]$. In the third example, we consider a part of a sphere singularly parametrized by

$$\begin{aligned} x &= \cos(\theta^2)\sin(\theta^1), \\ y &= \sin(\theta^2)\sin(\theta^1), \\ z &= \cos(\theta^1), \end{aligned} \tag{83}$$

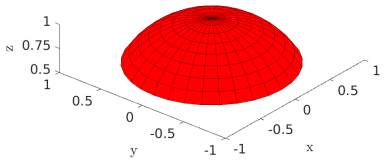

and $\theta^1 \in [0, 1]$ and $\theta^2 \in [0, 2\pi]$. In all three examples we choose for the thickness coordinate $\theta^3 \in [-0.05, 0]$. We use the material parameters of polyurethane given in Table 4 and an angular frequency $\omega = 20\,\mathrm{s}^{-1}$. For the construction of the manufactured solution, we take the structure of the shell model into account. Therefore, the solution is defined by specifying the parameters in (38) and (41). For the presented examples, these parameters are given in Table 1. The errors

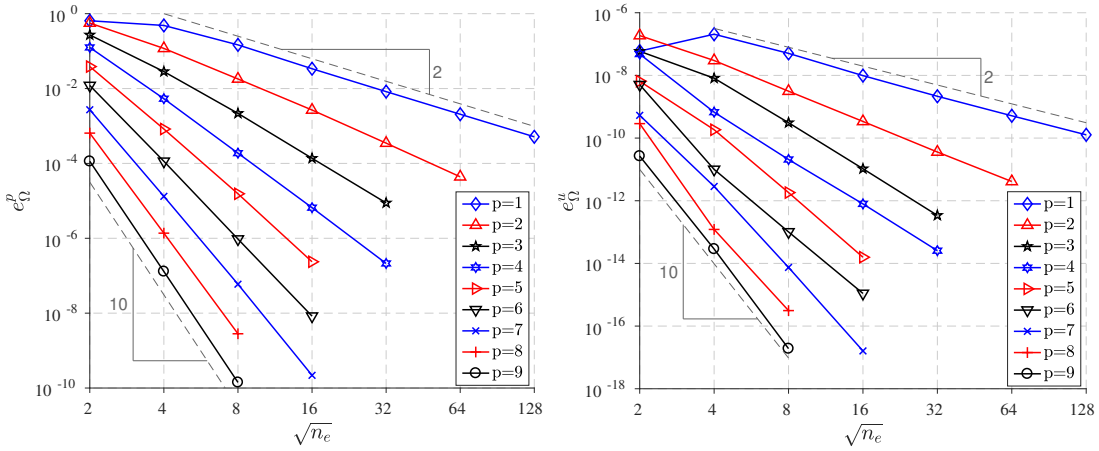

Figure 7: Example 1: pressure error e^p_Ω (left), displacement error e^u_Ω (right)

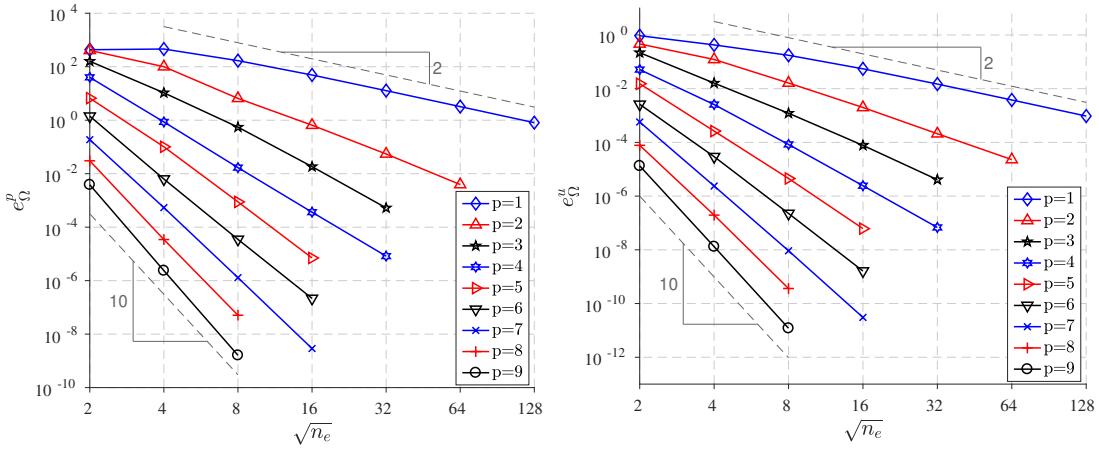

Figure 8: Example 2: pressure error e^p_Ω (left), displacement error e^u_Ω (right)

at multiple meshes with n_e elements each are illustrated in the Figures 7 to 9. In all graphs, the respective absolute error defined by

$$
\begin{aligned}
e^u_\Omega &= \sqrt{\int_\Omega (\mathbf{u}-\mathbf{u}^M)\cdot(\mathbf{u}-\mathbf{u}^M)\,\mathrm{d}\mathbf{x}}, \\
e^p_\Omega &= \sqrt{\int_\Omega (p-p^M)^2\,\mathrm{d}\mathbf{x}}
\end{aligned}
\tag{84}
$$

is plotted. Therein, $\mathbf{u}$ and p denote the numerical solution, whereas $\mathbf{u}^M$ and p^M denote the manufactured solutions. We observe the optimal convergence rate in all examples. Furthermore, we see from Figure 8 that a small discretization error in the displacement field leads to large error in the pressure field. This is due to the conditioning of the physical problem and depends on the material parameters. Therefore, we conclude that a accurate discretization of the displacement

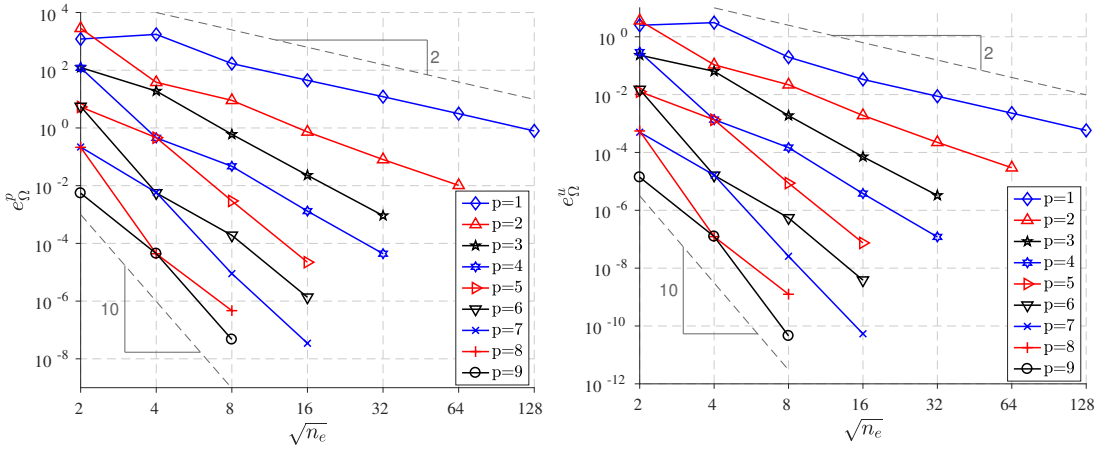

Figure 9: Example 3: pressure error e^p_Ω (left), displacement error e^u_Ω (right)

field is necessary in order to obtain an accurate pressure approximation.

Next, we discuss the results of the fourth verification example for the poro-elastic shell FEM in the case of an implicitly given reference surface. The considered spherical reference surface is given by $\phi = x^2 + y^2 + z^2 - 1$ and $B = [0,2]^3$. The shell volume has the extension t in the thickness direction and is symmetric around the reference surface. We prescribe the solution as

$$\mathbf{u}^M = \begin{bmatrix} xyz \\ xyz \\ xyz \end{bmatrix}, \tag{85}$$

and

$$p^M = xyz. \tag{86}$$

It is important to note that this solution cannot be exactly represented by the shell model. Therefore, a modeling error and a discretization error occurs. We use quintic shape functions for the discretization of a series of problems with decreasing thickness T. The results are depicted in Figure 10. We observe that the modeling error dominates in the case of thick shells. Therefore, a mesh refinement cannot reduce the overall error in this case. However, with decreasing thickness, the modeling error decreases and the discretization error dominates for the coarse meshes. In this regime, we observe the expected order of convergence of the FEM. In order to verify the layered shell theory we consider a fixed shell thickness $T = 0.2$ and use a varying number of layers n_L through-the-thickness and different numbers of finite elements. The results of the convergence study are depicted in Figure 11. With increasing number of layers the individual layer thickness t is reduced, which reduces the modeling error. We observe optimal quadratic convergence with respect to the layer thickness.

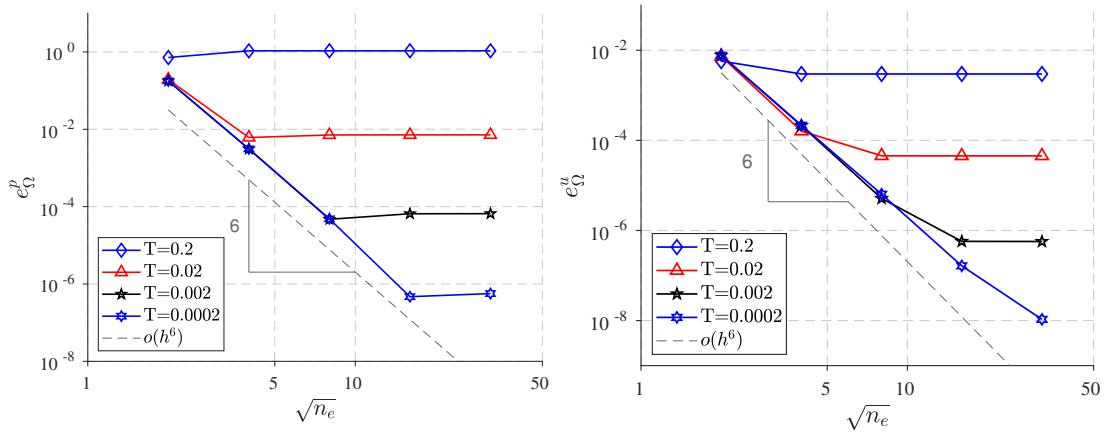

Figure 10: Example 4: pressure error e^p_Ω (left), displacement error e^u_Ω (right)

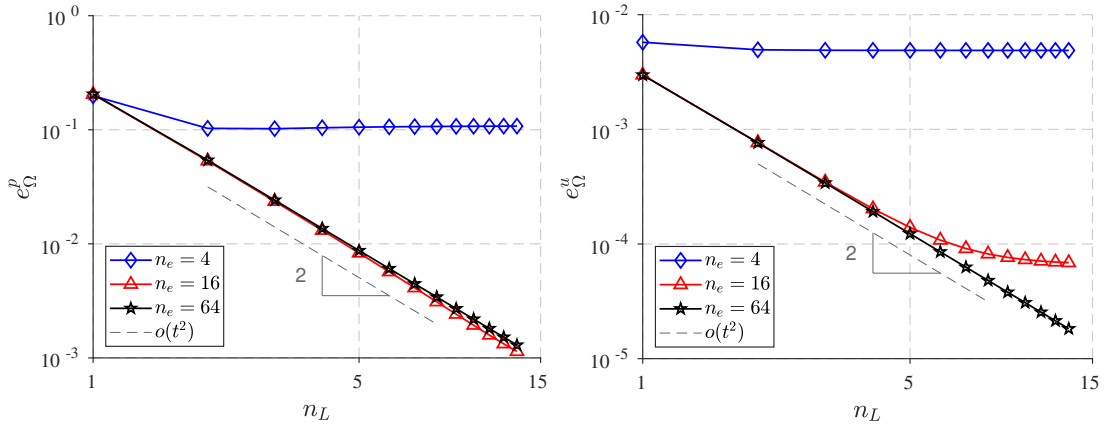

Figure 11: Example 4: pressure error e^p_Ω (left), displacement error e^u_Ω (right)

5.1.2 Verification of the MFS implementation

This section deals with the verification of the MFS for uncoupled acoustic fluid problems described in Section 4.2. To this end, we present the results of two examples. In both cases, the considered fluid is air with the material parameters given in Table 2.

In the first example, an interior problem is considered. The domain Ω^{int} is bounded by the plane $\partial\Omega_+$ and a parametrically given surface Γ,

$$\begin{aligned} x &= \cos(\theta^1)\sin(\theta^2), \\ y &= 2\sin(\theta^1)\sin(\theta^2), \\ z &= \frac{1}{2}\cos(\theta^2), \end{aligned} \tag{87}$$

where $\theta^1 \in [0, 2\pi]$ and $\theta^2 \in [0, \frac{\pi}{2}]$, see Figure 12. The constructed solution is obtained by means

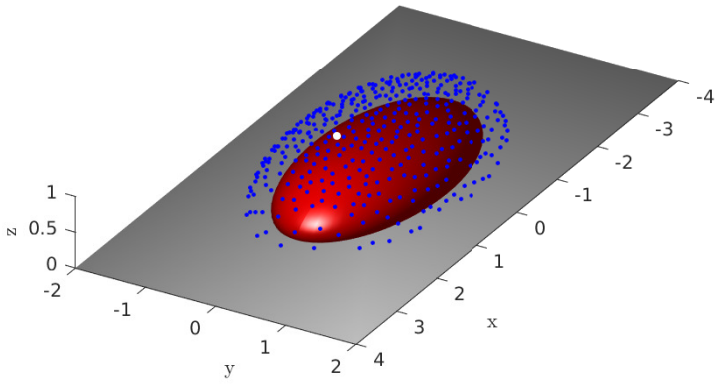

Figure 12: Configuration of the parametric MFS verification example: Sound hard plane at $z = 0$ (gray), sound hard surface Γ (red), MMS source point (white), MFS source points (blue)

of the fundamental solution. Therefore, we specify the point $\mathbf{y}_0 = [1\,\text{m},\ 0\,\text{m},\ 1\,\text{m}]$, which lies outside the problem domain. This defines the sought solution according to

$$p^M(\mathbf{x}) = \mathscr{G}(\mathbf{x}, \mathbf{y}_0) \qquad \text{for } \mathbf{x} \in \Omega^{\text{int}}. \tag{88}$$

The boundary data is derived from this solution as

$$g_N^M(\mathbf{x}) = \mathscr{H}(\mathbf{x}, \mathbf{y}_0) \cdot \mathbf{n}(\mathbf{x}) \qquad \text{for } \mathbf{x} \in \Gamma. \tag{89}$$

This boundary data is the input for the numerical method. The source points for the approximation are obtained by placing points on Γ and moving each 0.3 m in the direction normal to Γ.

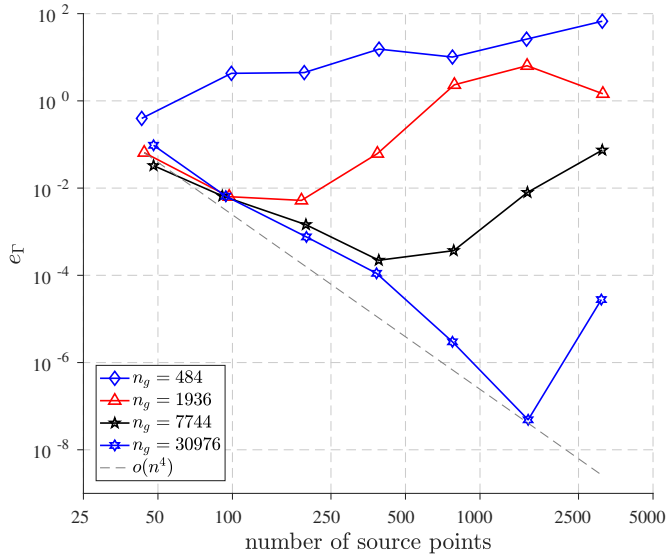

Figure 13: Error convergence for the parametric MFS verification example

The problem setting and a source point configuration are depicted in Figure 12. We investigate the acoustic problem at a frequency $f = 200\,\mathrm{Hz}$. In order to study the convergence behavior we introduce the relative error

$$e_\Gamma = \sqrt{\frac{\int_\Gamma (p^{\mathrm{M}} - p)^2 \,\mathrm{d}s_{\mathbf{x}}}{\int_\Gamma (p^{\mathrm{M}})^2 \,\mathrm{d}s_{\mathbf{x}}}}. \tag{90}$$

We evaluate this error for a number of solutions obtained with different number of source points. Furthermore, we study the influence of the numerical integration. The computed errors are plotted in Figure 13 for different number of quadrature points n_g used. It is evident that the integration has to be sufficiently accurate in order to obtain an accurate result. Therefore, one has to increase also the number of quadrature points when increasing the number of source points in order to obtain a monotonic convergence. Nevertheless, very accurate solutions are possible with only a few source points for the solution approximation.

In the second verification example, we consider an exterior problem. The unbounded problem domain is given as $\{(x,y,z)|\phi(x,y,z) > 0\} \cap \Omega_+$, where

$$\begin{aligned} \phi(x,y,z) = &\left(\left(x^2+y^2-1\right)^2 + \left(\frac{1}{2}+z\right)^2 \right) \times \\ &\times \left(x^2 + \left(\frac{25}{16}y^2 - 1 + \left(\frac{1}{5}+z\right)^2 \right)^2 \right) - \frac{4}{5}. \end{aligned} \tag{91}$$

The geometry of the problem and a source point configuration is depicted in Figure 14. We use $y_0 = [0.7\,\mathrm{m},\ 0.7\,\mathrm{m},\ 0.25\,\mathrm{m}]$ for the construction of the solution and the boundary data by means of (88) and (89). Again, we solve the acoustic problem at $f = 200\,\mathrm{Hz}$. The convergence behavior of the error (90) is plotted in Figure 15. We observe that the MFS is able to reproduce

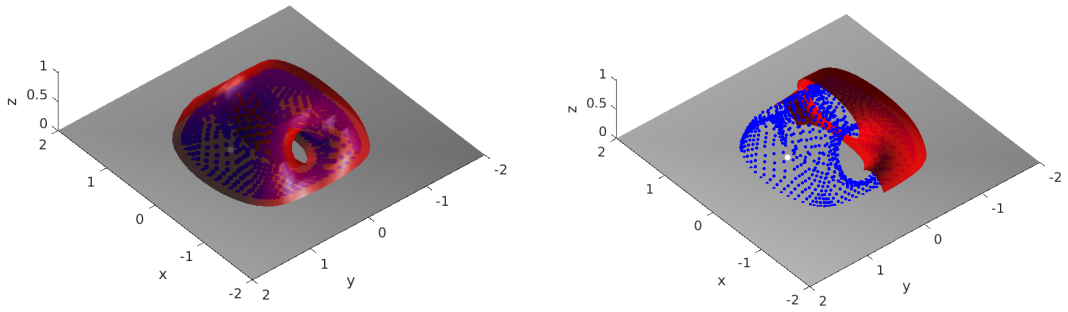

(a) Full model. (b) Structure cut at $y = 0$.

Figure 14: Configuration of the implicit MFS verification example: Sound hard plane at $z = 0$ (gray), sound hard surface Γ (red), MMS source point (white), MFS source points (blue)

the solution accurately in the case of this geometrically complex problem as well. As in the previous example, we see that a sufficient number of quadrature points is necessary in order to obtain stable results and a monotonic convergened method. Therefore, the number of source points and quadrature points has to be chosen with care, when applying the MFS.

5.1.3 Verification of the coupled method

In this section, we are concerned with the verification of the coupled MFS-FEM developed in Section 4.3. To this end, we consider radial symmetric problems, which allow for a closed form solution. Thus, we consider a spherical shell structure separating the upper half space into an interior and an exterior domain. The exact solutions of the three-dimensional problems are derived in Appendix B. In our FEM modell we approximate the spherical shell structure with a shell theory, hence, a modeling error is introduced.

The reference surface for the shell structure is a hemisphere with unit radius. First, we consider the case of an elastic aluminum structure with a thickness of $t = 0.025\,\mathrm{m}$. Therefore, the ratio of curvature radius and thickness is 40, classifying the structure as thin shell. The used material parameters are given in Table 3. In this example, an implicit geometry description of the hemisphere is used. The displacement of the shell is discretized with quartic finite element shape functions. The interior and exterior fluid pressure is discretized by means of the MFS. The error according to (90) is evaluated for the exterior acoustic fluid and plotted in Figure 16. The error is evaluated for varying finite element meshes and for varying number of MFS source points. The finite element meshes are identified by their number of elements n_e. Depending on the used discretization, the error is dominated either by the FEM or the MFS. For horizontal lines the error is dominated by the FEM discretization. This verifies the coupled method for the case of the acoustic fluid - elastic solid coupling.

Next, we consider a poro-elastic polyurethane shell structure separating the interior domain from the exterior domain. The material parameters are given in Table 4. The spherical shell is

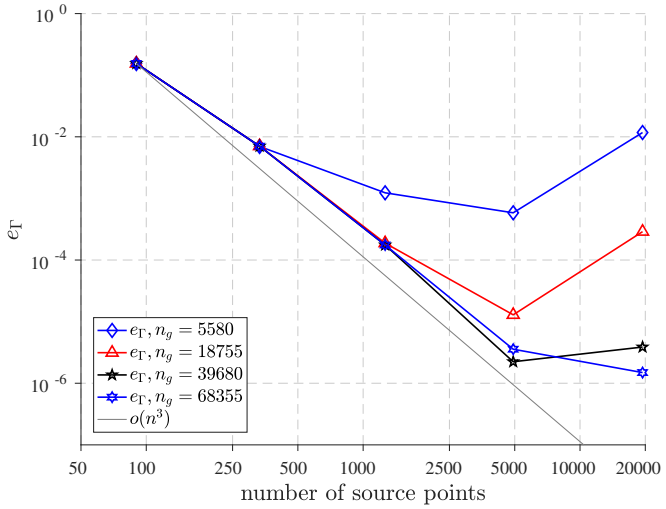

Figure 15: Error convergence for the implicit MFS verification example

described parametrically and has a thickness of $t = 0.002\,\mathrm{m}$. Quartic finite element shape functions are used for the discretization of the displacement and pressure field of the shell structure. The error according to (90) is evaluated for the exterior acoustic fluid and plotted in Figure 17. The numerical integration for all matrix entries is done on the finite elements. In the case of $n_e = 4$, we can see the instability, which arises due to the insufficient numerical integration. However, we do not observe such instability in the case of the other meshes. In the present example, we see that due to the modeling error the minimal achievable error is around 10^{-9}. Up to this error, we observe the convergence of the coupled method. Hence, this examples verifies the coupled method for the case of acoustic fluid $-$ poro-elastic solid coupling.

5.2 Sound transmission through poro-elastic shells

In the previous section, the implemented numerical methods were verified. Here, the capabilities of the developed methods are shown on the basis of more complex examples. We investigate the sound transmission from the inside of two cavities bounded by a poro-elastic shell structure to the outside. In one example the reference surface of the shell is given parametrically, whereas in the other it is given implicitly.

5.2.1 Deformed Sweep

In this example, we analyze a geometry which is given parametrically. We consider an ellipse which is moved along a circular path. Furthermore, the initial shape is deformed when moved. The initial ellipse lies in the $x-y$ plane with the center at $[0\,\mathrm{m}, 1\,\mathrm{m}, 0\,\mathrm{m}]$. The semi-major axis is $0.5\,\mathrm{m}$ in y direction, whereas the semi-major axis is $0.25\,\mathrm{m}$ in x direction. Finally, taking the

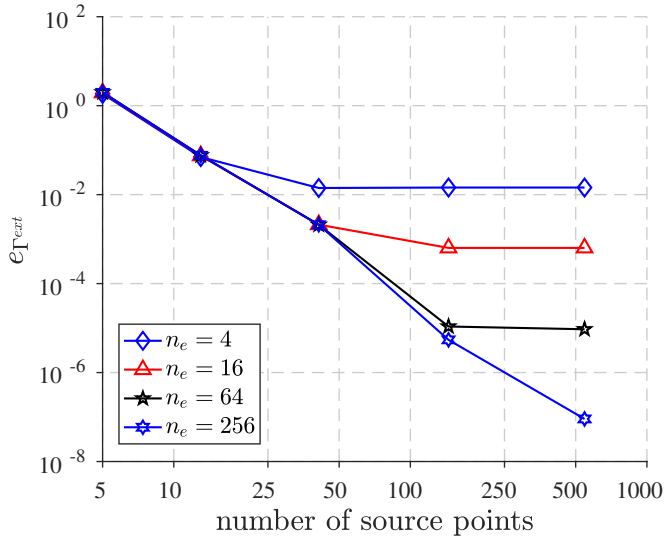

Figure 16: Error e_Γ for the exterior fluid in case of the coupled MFS-FEM: elastic structure and implicitly given reference surface

deformation into account, the reference surface is parametrically given by

$$\begin{aligned} x &= \frac{\cos(2\pi\theta^2)}{4}\left(\cos\left(\pi^2 f(\theta^1)\right)-2\right), \\ y &= \frac{\cos(\pi f(\theta^1))}{4}(4+2\sin(2\pi\theta^2)-\sin(\pi f(\theta^1))\sin(2\pi\theta^2)), \\ z &= \frac{\sin(\pi f(\theta^1))}{4}(4+2\sin(2\pi\theta^2)-\sin(\pi f(\theta^1))\sin(2\pi\theta^2)). \end{aligned} \tag{92}$$

with the mapping

$$f(\tau) = \tau((3-2\tau)\tau + b(1-3\tau+2\tau^2)), \quad b = \frac{1}{50}. \tag{93}$$

The parameter domain is $(\theta^1,\theta^2) \in [0,1]\times[0,1]$. In Figure 18, the geometry of the problem is visualized.

The shell structure is composed of two layers. We assign the material parameters of aluminum (see Table 3) to the first layer, which has a thickness of 0.01 m. The second layer is a poro-elastic polyurethane (see Table 4) layer with a thickness of 0.03 m. This poro-elastic layer is in contact with the interior fluid.

For the sake of solution verification, we consider the uncoupled dynamic response of the shell structure as a result of a surface load $\mathbf{t} = -\mathbf{e}_z 10^3\,\mathrm{N/m^2}$ applied on the free surface of the aluminum layer. For the analysis at 250 frequencies in the range $[0\,\mathrm{Hz}, 500\,\mathrm{Hz}]$ we use sextic ansatz functions. The vertical displacements u_z at the point $(\theta^1,\theta^2) = (0.5, 0.25)$ are plotted over the frequency in Figure 19 for three meshes (each mesh has n_e elements). For the better

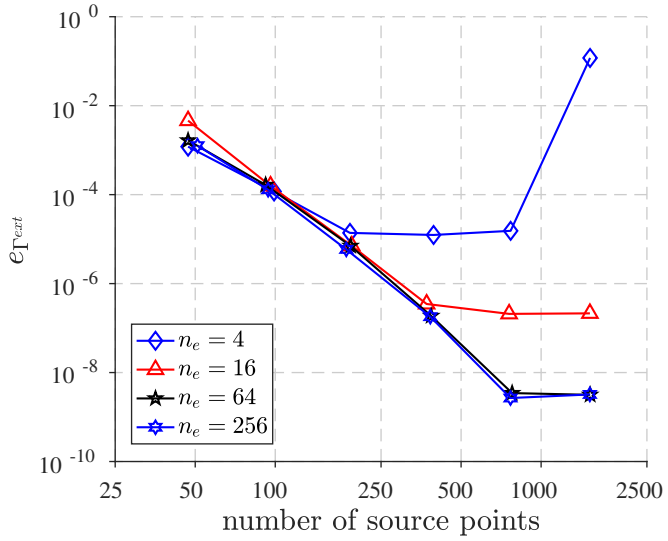

Figure 17: Error e_Γ for the exterior fluid in case of the coupled MFS-FEM: poro-elastic structure and parametrically given reference surface

visualization, we have used the logarithmic measure

$$L_p(u) = 10 \log_{10} \left(\frac{u^2}{4 \cdot 10^{-10}} \right) \text{dB}. \tag{94}$$

Due to these results, we will further use the 64-element mesh.

Next, the performance of the uncoupled MFS is studied. To this end, we calculate the interior pressure field due to a source with unit strength at the point $[0\,\text{m}, -1\,\text{m}, 0.5\,\text{m}]$. The structure is assumed to be rigid in this case. The exact solution to this problem has to be real-valued. In Figure 20, the imaginary part of the solutions at the evaluation point $[0\,\text{m}, 1\,\text{m}, 0.5\,\text{m}]$ obtained for a varying number of approximation source points are plotted. Based on this result, we proceed with 372 source points for the interior, as well as for the exterior fluid.

With the discretization described above, we study the sound transmission from the interior to the exterior. Again, we consider a source at the point $[0\,\text{m}, -1\,\text{m}, 0.5\,\text{m}]$ with unit strength for the excitation of the system. In Figure 21, the sound pressure level determined at the interior evaluation point $[0\,\text{m}, 1\,\text{m}, 0.5\,\text{m}]$ is plotted. We compare the cases *uncoupled MFS* (rigid structure), *aluminum shell* (only the aluminum layer) and *poro-elastic shell* (the aluminum layer with the polyurethane layer). The results for the cases *uncoupled MFS* and *aluminum shell* virtually agree. In the case of the *uncoupled MFS*, no dissipation occurs in the system and the solution is infinite at the eigenfrequencies. In the case of *aluminum shell* a small structural dissipation effect is present. This can be seen in Figure 21, where the eigenfrequencies are damped. However, we conclude that the compliance of the aluminum structure has only little influence on the interior sound pressure field. Nevertheless, the effects of the dissipation introduced by virtue of the

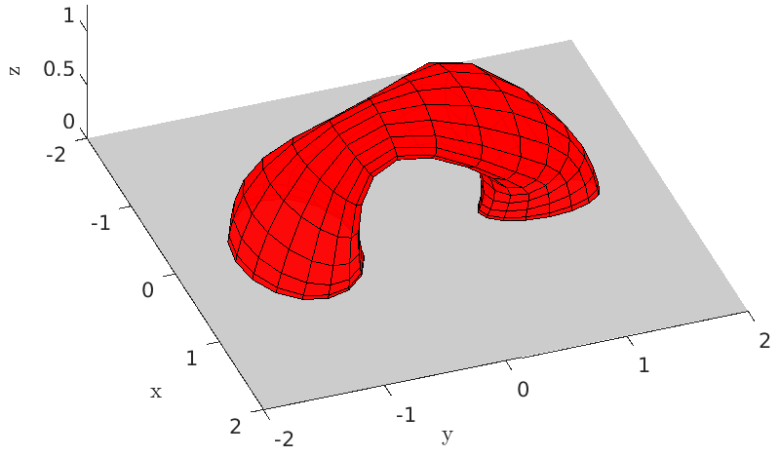

Figure 18: Geometry of the deformed sweep problem

poro-elastic polyurethane layer are clearly visible. In particular, the calculated sound pressure levels are significantly reduced for frequencies above $f = 200\,\mathrm{Hz}$. The same conclusion is valid for the results at the exterior evaluation point $[0\,\mathrm{m}, 0\,\mathrm{m}, 1.5\,\mathrm{m}]$. The sound pressure level determined at the exterior evaluation point $[0\,\mathrm{m}, 0\,\mathrm{m}, 1.5\,\mathrm{m}]$ is plotted over the frequency in Figure 22. In the case of an rigid structure no transmission can occur. Therefore, this case is not considered in Figure 22. Again, the sound pressure level is significantly reduced in the case *poro-elastic shell* compared to the case *aluminum shell*.

5.2.2 Sound transmission through an implicitly given shell

In this section, we consider the sound transmission through a shell structure described by an implicitly given reference surface. The corresponding level-set function is

$$\phi(x,y,z) = (2x)^4 + (2y)^2 + (2z)^2 - 0.25. \tag{95}$$

The geometry of the problem is depicted in Figure 23. The shell structure is composed of an aluminum (see Table 3) and a poro-elastic polyurethane layer (see Table 4). The aluminum layer is $t = 0.002\,\mathrm{m}$ thick, whereas the polyurethane layer has a thickness $t = 0.01\,\mathrm{m}$. The poro-elastic layer is in contact with the interior fluid.

In this example, we have chosen the discretization according to similar considerations made in Section 5.2.1. We use octic shape functions constructed on a 64-element mesh for the discretization of the parameters in the shell model. For the discretization of the interior and exterior fluid pressure fields, we use 145 MFS source points each. The sound pressure level at the interior evaluation point $[0\,\mathrm{m}, 0\,\mathrm{m}, 0.1\,\mathrm{m}]$ due to a source at the point $[-0.25\,\mathrm{m}, -0.05\,\mathrm{m}, 0.1\,\mathrm{m}]$ with unit strength is plotted in Figure 24. Therein, the case of a rigid structure (uncoupled MFS), an aluminum shell and the full poro-elastic structure is considered. We conclude that the compliance of the aluminum structure has only little influence on the interior sound pressure field. However, the effects of the dissipation introduced by virtue of the poro-elastic layer are visible.

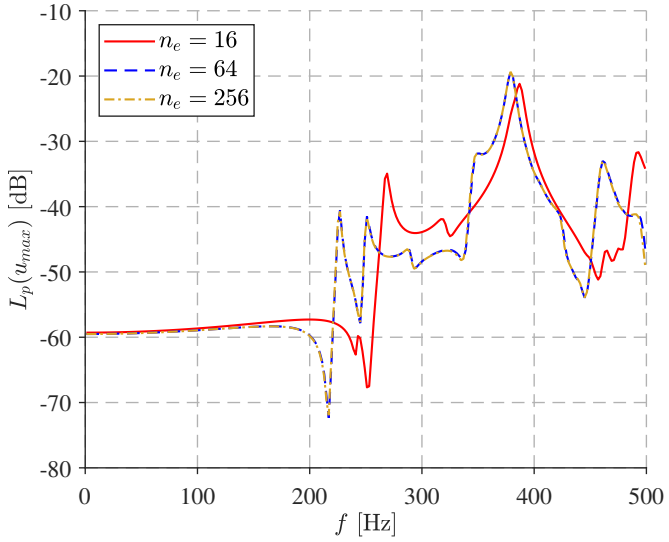

Figure 19: Deformed sweep problem: Vertical displacement u_z at point $(\theta^1, \theta^2) = (0.5, 0.25)$ of the uncoupled shell problem

The same conclusion is valid for the results at the exterior evaluation point $[0\,\text{m}, 0\,\text{m}, 0.3\,\text{m}]$, see Figure 25.

6 Conclusions

We have presented a new simulation method for vibro-acoustic analysis. In particular, we have treated the simulation of laminated poro-elastic shell structures and their interaction with the surrounding fluid. In order to face this complicated situation, a layer-wise shell model has been developed. The through-the-thickness variation of the displacement field is described by a seven-parameter model, which is assumed in each layer. The pressure field occurring only in the poro-elastic layers is described with a quadratic expansion through-the-thickness.

The numerical model consists of a FEM formulation for the shell and the MFS for the acoustic domains. Hence, the radiation condition is implicitly fulfilled by the MFS due to the usage of the acoustic fundamental solutions. The FEM for the shell is based on the exact geometry given by either a parametric or an implicit representation of the reference surface. In the case of a given parametrization, the evaluation of the quantities from differential geometry are done with respect to this parametrization and not with respect to a superfluous geometry discretization. In the case of an implicitly defined surface, the exact parametrization is constructed by means of the level-set function. Contrary to most MFS solutions, here, the strength of the sources for the field approximation are determined by a variational formulation. This has the advantage that the need of collocation points is circumvented.

The implemented numerical methods are verified against solutions obtained from the method of manufactured solutions. In this method, a distinct solution is chosen and the corresponding source terms and boundary conditions are derived from the chosen solution. For the devel-

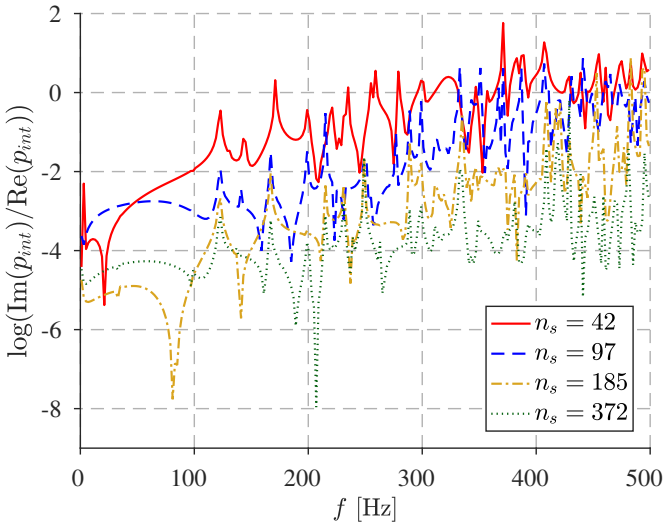

Figure 20: Deformed sweep problem: Imaginary part of the uncoupled MFS solution

oped shell FEM, this approach has been implemented in the curvilinear coordinates induced by the shell geometry. For the verification of the MFS, the prescribed solution is constructed by a fundamental solution. Thus, the FEM and the MFS could be verified with high rigor. The coupled method has been verified against radial symmetric problems. The reference solutions were obtained by solving these problems analytically. The calculation of the sound transmission through geometrically complicated layered shells structure has shown the suitability of the proposed approach for real world examples.

A Material parameter

The material parameters used in the numerical examples are summarized in the following tables.

bulk modulus $K\left[\mathrm{kN}/\mathrm{m}^2\right]$	$1.01 \cdot 10^5$
density $\rho\left[\mathrm{kg}/\mathrm{m}^3\right]$	1.205

Table 2: Material parameter of air

B Radial symmetric solutions

We derive radial symmetric solutions of two coupled problems. In both cases a spherical shell structure separates a bounded interior fluid domain from an unbounded exterior fluid domain. In particular, we consider the cases *acoustic fluid - elastic layer - acoustic fluid* and

Young's modulus $E[\mathrm{N/m^2}]$	$70 \cdot 10^9$
Poisson's ratio $\nu[-]$	0.3
density $\rho[\mathrm{kg/m^3}]$	2700
loss factor $\eta[-]$	0.01

Table 3: Material parameter of aluminum

Young's modulus $E[\mathrm{N/m^2}]$	$70 \cdot 10^3$
Poisson's ratio $\nu[-]$	0.39
density $\rho[\mathrm{kg/m^3}]$	22.1
loss factor $\eta[-]$	0.265
porosity $\phi[-]$	0.98
static flow resistivity $\sigma[\mathrm{kg/m^3 s}]$	3750
tortuosity $\alpha_\infty[-]$	1.17
viscous length $\Lambda[\mu m]$	110
thermal length $\Lambda'[\mu m]$	742

Table 4: Material parameter of a polyurethane foam [32]

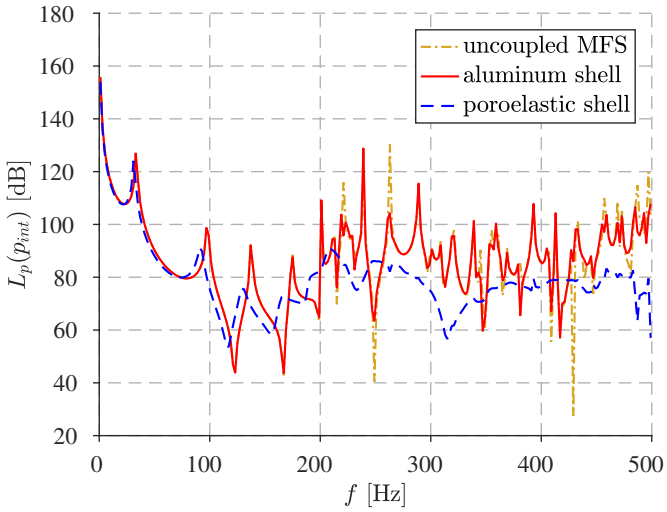

Figure 21: Deformed sweep problem: Comparison of the sound pressure level at the interior evaluation point for elastic and poro-elastic shell

acoustic fluid - poro − elastic layer - acoustic fluid. We employ the spherical coordinates (r, φ, γ). Thus,

$$\begin{aligned} x &= r\cos(\varphi)\cos(\gamma) \\ y &= r\sin(\varphi)\cos(\gamma) \\ z &= r\sin(\gamma). \end{aligned} \tag{96}$$

Acoustic fluid The Helmholtz equation in spherical coordinates assuming radial symmetry $(p(r,\varphi,\gamma) = p(r))$ reads

$$k^2 p + \frac{\partial^2 p}{\partial r^2} + \frac{2}{r}\frac{\partial p}{\partial r} = 0. \tag{97}$$

By setting $r = \frac{x}{k}$, we obtain

$$x^2 \frac{d^2 y}{dx^2} + 2x\frac{dy}{dx} + [x^2 - n(n+1)]y = 0 \tag{98}$$

with $n = 0$. The solutions for $n \in \mathbb{N}$ are the Spherical Bessel functions $j_n(x)$ and $y_n(x)$. For the case $n = 0$, they are

$$j_0(x) = \frac{\sin(x)}{x} \quad \text{and} \quad y_0(x) = \frac{-\cos(x)}{x}. \tag{99}$$

Thus, solutions of (97) are of the form

$$p(r) = a_1\, j_0(kr) + a_2\, y_0(kr), \tag{100}$$

where a_1, a_2 are constants, which have to be adapted to the respective problem. The radial displacement of the acoustic fluid is given by

$$u^a(r) = \frac{p_{,r}}{\omega^2 \rho^a}. \tag{101}$$

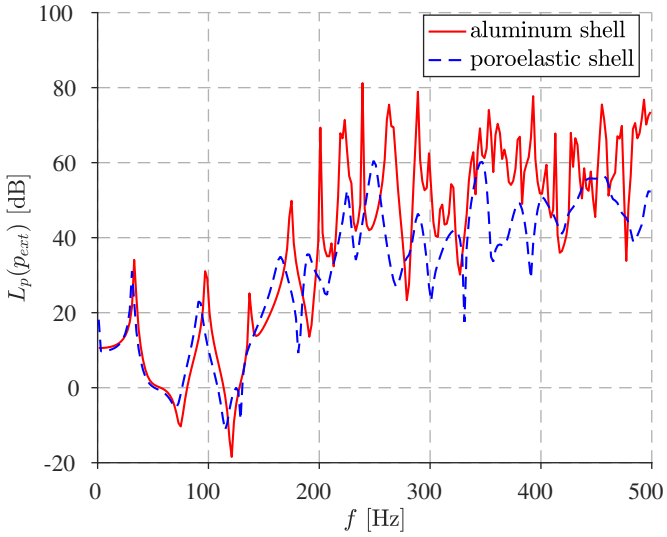

Figure 22: Deformed sweep problem: Comparison of the sound pressure level at the exterior evaluation point for elastic and poro-elastic shell

Elastodynamics The equations of motion for a elastic solid in spherical coordinates assuming radial symmetry ($\mathbf{u}(r,\varphi,\gamma) = \mathbf{e}_r u(r)$) reduce to [1]

$$\frac{\partial \sigma_{rr}}{\partial r} + \frac{1}{r}(2\sigma_{rr} - \sigma_{\theta\theta} - \sigma_{\phi\phi}) = -\omega^2 \rho\, u_r. \tag{102}$$

The stress components are given by

$$\begin{aligned} \sigma_{rr} &= (\lambda + 2\mu)\frac{\partial u}{\partial r} + 2\lambda\frac{u}{r}, \\ \sigma_{\theta\theta} = \sigma_{\phi\phi} &= \lambda\frac{\partial u}{\partial r} + 2\lambda\frac{u}{r} + 2\mu\frac{u}{r}. \end{aligned} \tag{103}$$

Inserting (103) in (102) yields

$$\frac{\partial^2 u}{\partial r^2} + \frac{2}{r}\frac{\partial u}{\partial r} + \left(\frac{\omega^2}{c^2} - \frac{2}{r^2}\right) u = 0 \tag{104}$$

with $c = \sqrt{\frac{\lambda+2\mu}{\rho}}$. Multiplying with r^2 and $\Lambda^2 = \frac{\omega^2}{c^2}$ gives

$$r^2\frac{\partial^2 u}{\partial r^2} + 2r\frac{\partial u}{\partial r} + \left(\Lambda^2 r^2 - 2\right) u = 0. \tag{105}$$

By setting $r = \frac{x}{\Lambda}$, we obtain

$$x^2\frac{\partial^2 u}{\partial x^2} + 2x\frac{\partial u}{\partial x} + \left(x^2 - 2\right) u = 0, \tag{106}$$

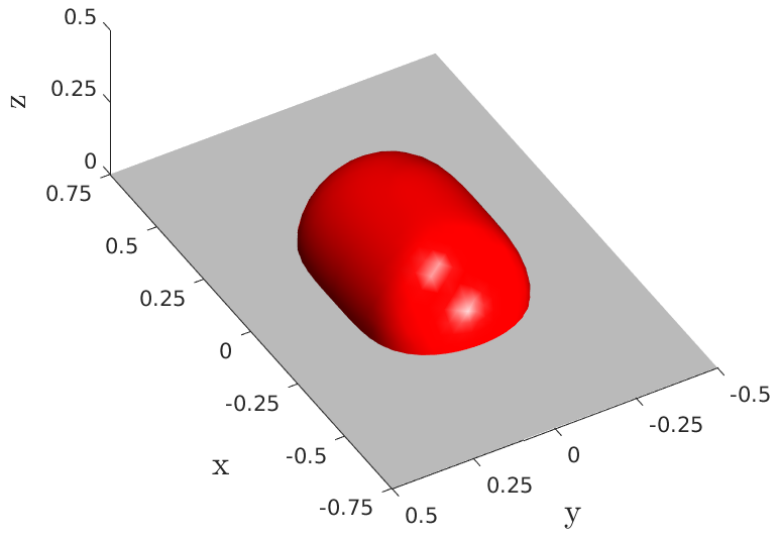

Figure 23: Geometry of the implicitly given shell

which is in accordance with (98) for $n = 1$. Therefore, the solutions are

$$j_1(x) = \frac{\sin(x)}{x^2} - \frac{\cos(x)}{x} \quad , \quad y_1(x) = -\frac{\cos(x)}{x^2} - \frac{\sin(x)}{x}. \tag{107}$$

Thus, the radial symmetric displacement field is of the form

$$u^e(r) = b_1\, j_1(kr) + b_2\, y_1(kr), \tag{108}$$

with the two constants b_1 and b_2.

Poroelasticity For the derivation of the poro-elastic spherical radial symmetric solution, we follow [48]. The governing equations are

$$M\frac{\partial}{\partial r}\left(\frac{1}{r^2}\frac{\partial}{\partial r}\left(r^2 u\right)\right) - (\alpha+\beta)\frac{\partial p}{\partial r} + \omega^2(\rho+\beta\rho_f)\, u = 0 \tag{109}$$

and

$$-\frac{\beta}{\omega^2\rho_f}\Delta p + (\beta+\alpha)\,\nabla\cdot u + \frac{\phi^2}{R}p = 0. \tag{110}$$

Defining the displacement potential $u = \frac{\partial\Phi}{\partial r}$ leads to

$$\frac{\partial}{\partial r}\left[M\left(\frac{1}{r^2}\frac{\partial}{\partial r}\left(r^2\frac{\partial\Phi}{\partial r}\right)\right) - (\alpha+\beta)\, p + \omega^2(\rho+\beta\rho_f)\,\Phi\right] = 0 \tag{111}$$

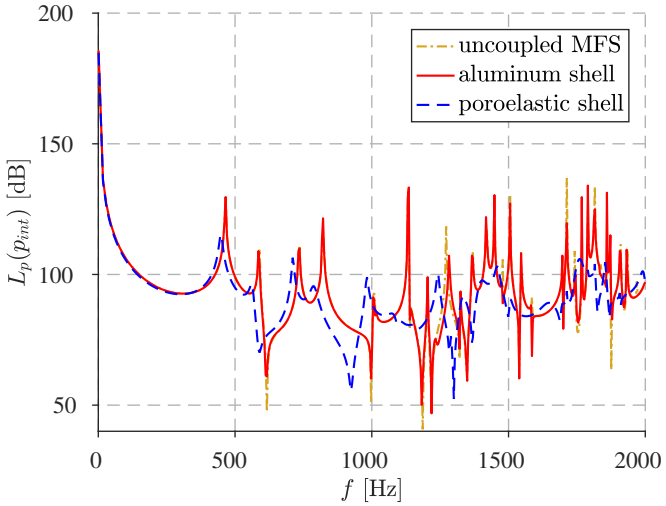

Figure 24: Comparison of the sound pressure level at the interior evaluation point for the aluminium and the poro-elastic shell

Furthermore, we set $\Phi = \frac{\xi}{r}$ and $p = \frac{\chi}{r}$ to obtain

$$\begin{aligned} \xi_{,rr} - \frac{\alpha+\beta}{M}\chi + \frac{\omega^2(\rho+\beta\rho_f)}{M}\xi = 0, \\ \frac{\beta}{\omega^2\rho_f}\chi_{,rr} + (\alpha+\beta)\,\xi_{,rr} + \frac{\phi^2}{R}\chi = 0. \end{aligned} \tag{112}$$

The ansatz

$$\begin{aligned} \xi = \xi_i \mathrm{e}^{\omega\Lambda_i r}, \\ \chi = \chi_i \mathrm{e}^{\omega\Lambda_i r} \end{aligned} \tag{113}$$

leads to the system of equations

$$\begin{bmatrix} \omega^2(\Lambda^2 + \frac{\rho+\beta\rho_f}{M}) & \frac{(\alpha+\beta)}{M} \\ \omega^2\Lambda^2(\alpha+\beta) & \frac{\beta\Lambda^2}{\rho_f} + \frac{\phi^2}{R} \end{bmatrix} \begin{bmatrix} \xi_i \\ \chi_i \end{bmatrix} = \begin{bmatrix} 0 \\ 0 \end{bmatrix}. \tag{114}$$

The four roots of the characteristic equation are found to be

$$\begin{aligned} \Lambda_1 = -\Lambda_2 = \frac{\sqrt{-A + \sqrt{A^2 - 4B}}}{\sqrt{2}}, \\ \Lambda_3 = -\Lambda_4 = \frac{\sqrt{-A - \sqrt{A^2 - 4B}}}{\sqrt{2}}, \end{aligned} \tag{115}$$

where

$$\begin{aligned} A = -\frac{\rho_f\phi^2}{\beta R} - \frac{\rho_f(\alpha+\beta)^2}{\beta M} + \frac{\rho+\beta\rho_f}{M}, \\ B = -\frac{\rho_f\phi^2(\rho+\beta\rho_f)}{\beta MR}. \end{aligned} \tag{116}$$

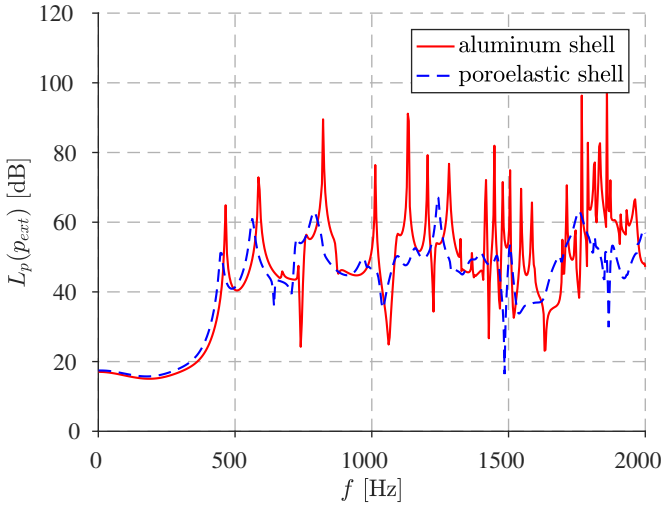

Figure 25: Comparison of the sound pressure level at the exterior evaluation point for the aluminium and the poro-elastic shell

Furthermore, $\chi_i = -\frac{\omega^2}{\alpha+\beta}(\lambda_i^2 M + \rho + \beta\rho_f)\xi_i$. Thus, the homogeneous solution has the form

$$\begin{aligned} u(r) &= \sum_{i=1}^{4} \xi_i \left(\omega\lambda_i - \frac{1}{r}\right) \frac{\mathrm{e}^{\omega\lambda_i r}}{r}, \\ p(r) &= \sum_{i=1}^{4} -\frac{\omega^2}{\alpha+\beta}(\lambda_i^2 M + \rho + \beta\rho_f)\xi_i \frac{\mathrm{e}^{\omega\lambda_i r}}{r}. \end{aligned} \tag{117}$$

Here, we have four constants ξ_i, which have to be determined. We remark that the total radial stress is given by

$$\sigma_{rr}^{\mathrm{tot}}(r) = (\lambda + 2\mu)\frac{\partial u(r)}{\partial r} + 2\lambda\frac{u(r)}{r} - \alpha p(r). \tag{118}$$

Coupled Solutions. The unknown coefficients introduced above can be determined, if the boundary and coupling conditions are taken into account. We state them for the two cases used in Section 5.1.3. These cases are the *acoustic fluid - elastic layer - acoustic fluid* and *acoustic fluid - poro − elastic layer - acoustic fluid* problems. Thus, we have two acoustic fluid domains and two material interfaces in both domains. The pressure solutions of the interior domain and the exterior domain are denoted by p^{int} and p^{ext}, respectively. The material interfaces are located at the fixed radii r^{int} and r^{ext}. The excitation is given by an acoustic point source placed at the origin. Thus, we make the ansatz

$$p^{int} = \frac{\cos(kr)}{r} a^{int} + \frac{\mathrm{e}^{-\mathrm{i}kr}}{4\pi r}, \tag{119}$$

where we considered the non-singular part in (100). In order to fulfill the Sommerfeld radiation condition, we set $a_2 = -a_1 = a^{ext}$ in (100) and write

$$p^{ext} = \frac{\cos(kr) - \mathrm{i}\sin(kr)}{r}\, a^{ext}. \tag{120}$$

The interface conditions for the acoustic fluid - elastic solid interfaces are given by

$$\begin{aligned} p^{int}(r^{int}) &= \sigma_{rr}(r^{int}), \\ u^{int}(r^{int}) &= u^{e}(r^{int}), \\ p^{ext}(r^{ext}) &= \sigma_{rr}(r^{ext}), \\ u^{ext}(r^{ext}) &= u^{e}(r^{ext}). \end{aligned} \tag{121}$$

Therefore, the unknown constants a^{int}, a^{ext} and b_1, b_2 in (108) can be determined. The respective conditions for the acoustic fluid $-$ poro-elastic solid interfaces are

$$\begin{aligned} p^{int}(r^{int}) &= \sigma_{rr}^{\mathrm{tot}}(r^{int}), \\ p^{int}(r^{int}) &= p(r^{int}), \\ u^{int}(r^{int}) &= u^{p}(r^{int}), \\ p^{ext}(r^{ext}) &= \sigma_{rr}^{\mathrm{tot}}(r^{ext}), \\ p^{ext}(r^{ext}) &= p(r^{ext}), \\ u^{ext}(r^{ext}) &= u^{p}(r^{ext}). \end{aligned} \tag{122}$$

These conditions allow to uniquely determine the six coefficients a^{int}, a^{ext} and ξ_i in this case. We have used the computer algebra system Mathematica [68] for this task.

References

[1] Jan Achenbach. *Wave propagation in elastic solids*, volume 16. Elsevier, 2012.

[2] Jean Allard and Noureddine Atalla. *Propagation of sound in porous media*. John Wiley & Sons, 2nd edition, 2009.

[3] Paulo Amado-Mendes, Pedro Alves Costa, Luís MC Godinho, and Patrícia Lopes. 2.5D MFS-FEM model for the prediction of vibrations due to underground railway traffic. *Engineering Structures*, 104:141–154, 2015.

[4] RA Arciniega and JN Reddy. Tensor-based finite element formulation for geometrically nonlinear analysis of shell structures. *Computer Methods in Applied Mechanics and Engineering*, 196(4):1048–1073, 2007.

[5] Matthias Albert Augustin. *A method of fundamental solutions in poroelasticity to model the stress field in geothermal reservoirs*. Birkhäuser, 2015.

[6] Maurice A Biot. Theory of propagation of elastic waves in a fluid-saturated porous solid. I. Low-frequency range. *The Journal of the Acoustical Society of America*, 28(2):168–178, 1956.

[7] Maurice A Biot. Theory of propagation of elastic waves in a fluid-saturated porous solid. II. Higher frequency range. *The Journal of the Acoustical Society of America*, 28(2):179–191, 1956.

[8] Manfred Bischoff and Ekkehard Ramm. On the physical significance of higher order kinematic and static variables in a three-dimensional shell formulation. *International Journal of Solids and Structures*, 37(46-47):6933–6960, 2000.

[9] Marc Bonnet. *Boundary integral equation methods for solids and fluids*. John Wiley & Sons, 1995.

[10] Marc Bonnet. *Boundary integral equation methods for solids and fluids*. John Wiley, 1995.

[11] Jakub Wiktor Both, Manuel Borregales, Jan Martin Nordbotten, Kundan Kumar, and Florin Adrian Radu. Robust fixed stress splitting for Biot's equations in heterogeneous media. *Applied Mathematics Letters*, 68:101 – 108, 2017.

[12] Erik Burman, Susanne Claus, Peter Hansbo, Mats G Larson, and André Massing. CutFEM: Discretizing geometry and partial differential equations. *International Journal for Numerical Methods in Engineering*, 104(7):472–501, 2015.

[13] Mauricio F Caliri, Antonio JM Ferreira, and Volnei Tita. A review on plate and shell theories for laminated and sandwich structures highlighting the finite element method. *Composite Structures*, 156:63–77, 2016.

[14] Yvan Champoux and Jean-F Allard. Dynamic tortuosity and bulk modulus in air-saturated porous media. *Journal of Applied Physics*, 70(4):1975–1979, 1991.

[15] Dominique Chapelle and Klaus-Jurgen Bathe. *The finite element analysis of shells*. Springer Science & Business Media, 2010.

[16] Leilei Chen, Changjun Zheng, and Haibo Chen. Fem/wideband fmbem coupling for structural–acoustic design sensitivity analysis. *Computer Methods in Applied Mechanics and Engineering*, 276:1–19, 2014.

[17] Monique Dauge, Erwan Faou, and Zohar Yosibash. Plates and shells: Asymptotic expansions and hierarchic models. *Encyclopedia of Computational Mechanics*, 2004.

[18] Elke Deckers, Onur Atak, Laurens Coox, Roberto D'Amico, Hendrik Devriendt, Stijn Jonckheere, Kunmo Koo, Bert Pluymers, Dirk Vandepitte, and Wim Desmet. The wave based method: An overview of 15 years of research. *Wave Motion*, 51(4):550–565, 2014.

[19] Elke Deckers, Stijn Jonckheere, Dirk Vandepitte, and Wim Desmet. Modelling techniques for vibro-acoustic dynamics of poroelastic materials. *Archives of Computational Methods in Engineering*, 22(2):183–236, 2015.

[20] Alan Demlow. Higher-order finite element methods and pointwise error estimates for elliptic problems on surfaces. *SIAM Journal on Numerical Analysis*, 47(2):805–827, 2009.

[21] Wim Desmet. *A wave based prediction technique for coupled vibro-acoustic analysis*. PhD thesis, Katholieke Universiteit Leuven, Belgique, 1998.

[22] Emmanuel Detournay and Alexander H-D Cheng. Fundamentals of poroelasticity. In C Fairhurst, editor, *Comprehensive Rock Engineering: Principles, Practice and Projects, Analysis and Design Methods*, volume 2, pages 113–171. 1993.

[23] Alexander Düster, Henrike Bröker, and Ernst Rank. The p-version of the finite element method for three-dimensional curved thin walled structures. *International Journal for Numerical Methods in Engineering*, 52(7):673–703, 2001.

[24] Graeme Fairweather, Andreas Karageorghis, and Paul A Martin. The method of fundamental solutions for scattering and radiation problems. *Engineering Analysis with Boundary Elements*, 27(7):759–769, 2003.

[25] Denny Fritze, Steffen Marburg, and Hans-Jürgen Hardtke. FEM–BEM-coupling and structural–acoustic sensitivity analysis for shell geometries. *Computers & Structures*, 83 (2):143–154, 2005.

[26] MH Gfrerer and M Schanz. Code verification examples based on the method of manufactured solutions for kirchhoff–love and reissner–mindlin shell analysis. *Engineering with Computers*, 34(4):775–785, 2018.

[27] MH Gfrerer and Martin Schanz. A high-order fem with exact geometry description for the laplacian on implicitly defined surfaces. *International journal for numerical methods in engineering*, 114(11):1163–1178, 2018.

[28] Michael Helmut Gfrerer. *Vibro-acoustic simulation of poroelastic shells*. Monographic Series TU Graz, Computation in Engineering and Science, 2018.

[29] Michael Helmut Gfrerer and Martin Schanz. High order exact geometry finite elements for seven-parameter shells with parametric and implicit reference surfaces. *Computational mechanics*, 64(1):133–145, 2019.

[30] L Godinho, P Amado-Mendes, A Pereira, and D Soares. A coupled MFS–FEM model for 2-D dynamic soil–structure interaction in the frequency domain. *Computers & Structures*, 129:74–85, 2013.

[31] Ralf Hiptmair, Andrea Moiola, and Ilaria Perugia. A survey of trefftz methods for the helmholtz equation. In *Building Bridges: Connections and Challenges in Modern Approaches to Numerical Partial Differential Equations*, pages 237–278. Springer, 2016.

[32] N-E Hörlin, M Nordström, and Peter Göransson. A 3-D hierarchical FE formulation of Biot's equations for elasto-acoustic modelling of porous media. *Journal of Sound and Vibration*, 245(4):633–652, 2001.

[33] David Linton Johnson, Joel Koplik, and Roger Dashen. Theory of dynamic permeability and tortuosity in fluid-saturated porous media. *Journal of Fluid Mechanics*, 176:379–402, 1987.

[34] Stijn Jonckheere, Elke Deckers, Bert Van Genechten, Dirk Vandepitte, and Wim Desmet. A direct hybrid Finite Element–Wave Based Method for the steady-state analysis of acoustic cavities with poro-elastic damping layers using the coupled Helmholtz–Biot equations. *Computer Methods in Applied Mechanics and Engineering*, 263:144–157, 2013.

[35] Eisuke Kita and Norio Kamiya. Trefftz method: An overview. *Advances in Engineering Software*, 24(1):3–12, 1995.

[36] Frank Koschnick. *Geometrische Lockingeffekte bei Finiten Elementen und ein allgemeines Konzept zu ihrer Vermeidung*. Shaker, 2004.

[37] Joong Seok Lee, Elke Deckers, Stijn Jonckheere, Wim Desmet, and Yoon Young Kim. A direct hybrid finite element–wave based modelling technique for efficient analysis of poroelastic materials in steady-state acoustic problems. *Computer Methods in Applied Mechanics and Engineering*, 304:55–80, 2016.

[38] Nicholas Malaya, Kemelli C Estacio-Hiroms, Roy H Stogner, Karl W Schulz, Paul T Bauman, and Graham F Carey. Masa: a library for verification using manufactured and analytical solutions. *Engineering with Computers*, 29(4):487–496, 2013.

[39] Anna Marciniak-Czochra and Andro Mikelić. A rigorous derivation of the equations for the clamped Biot-Kirchhoff-Love poroelastic plate. *Archive for Rational Mechanics and Analysis*, 215(3):1035–1062, 2015.

[40] Onofre Marco, Ruben Sevilla, Yongjie Zhang, Juan José Ródenas, and Manuel Tur. Exact 3D boundary representation in finite element analysis based on Cartesian grids independent of the geometry. *International Journal for Numerical Methods in Engineering*, 2015.

[41] Andro Mikelic and Josip Tambaca. Derivation of a poroelastic flexural shell model. *Multiscale Modeling & Simulation*, 14(1):364–397, 2016.

[42] Andro Mikelić and Mary F. Wheeler. Convergence of iterative coupling for coupled flow and geomechanics. *Computational Geosciences*, 17(3):455–461, 2013.

[43] L. Nagler and M. Schanz. An extendable poroelastic plate formulation in dynamics. *Archive of Applied Mechanics*, 80:1177–1195, 2010.

[44] Loris Nagler, Ping Rong, Martin Schanz, and Otto von Estorff. Sound transmission through a poroelastic layered panel. *Computational Mechanics*, 53(4):549–560, 2014.

[45] Benoit Nennig, Emmanuel Perrey-Debain, and J-D Chazot. The method of fundamental solutions for acoustic wave scattering by a single and a periodic array of poroelastic scatterers. *Engineering Analysis with Boundary Elements*, 35(8):1019–1028, 2011.

[46] William L Oberkampf and Christopher J Roy. *Verification and validation in scientific computing*. Cambridge University Press, 2010.

[47] J Tinsley Oden, Ted Belytschko, Jacob Fish, TJ Hughes, Chris Johnson, David Keyes, Alan Laub, Linda Petzold, David Srolovitz, and S Yip. Revolutionizing engineering science through simulation. *National Science Foundation Blue Ribbon Panel Report*, 65, 2006.

[48] Mehmet Ozyazicioglu. Sudden pressurization of a spherical cavity in a poroelastic medium. *Mathematical Problems in Engineering*, 2013, 2013.

[49] Jamshid Parvizian, Alexander Düster, and Ernst Rank. Finite cell method. *Computational Mechanics*, 41(1):121–133, 2007.

[50] Paulo Mattos Pimenta and Eduardo Morais Barreto Campello. Shell curvature as an initial deformation: A geometrically exact finite element approach. *Int J Numer Methods Eng*, 78(9):1094–1112, 2009.

[51] E Rank, A Düster, V Nübel, K Preusch, and OT Bruhns. High order finite elements for shells. *Computer Methods in Applied Mechanics and Engineering*, 194(21):2494–2512, 2005.

[52] Ernst Rank, Stefan Kollmannsberger, Ch Sorger, and Alexander Düster. Shell finite cell method: A high order fictitious domain approach for thin-walled structures. *Computer Methods in Applied Mechanics and Engineering*, 200(45):3200–3209, 2011.

[53] Douglas D Reynolds. *Engineering principles of acoustics: Noise and vibration control*. Allyn & Bacon, 1981.

[54] Patrick J Roache. *Verification and validation in computational science and engineering*. Hermosa, 1998.

[55] P. Rong, O. v. Estorff, L. Nagler, and M. Schanz. An acoustical finite shell element for the simulation of air layers. *Journal of Computational Acoustics*, 21(4):1350014, 2013. doi: 10.1142/S0218396X13500148.

[56] Christopher J Roy. Review of code and solution verification procedures for computational simulation. *Journal of Computational Physics*, 205(1):131–156, 2005.

[57] Thomas Rüberg, Fehmi Cirak, and José Manuel García Aznar. An unstructured immersed finite element method for nonlinear solid mechanics. *Advanced Modeling and Simulation in Engineering Sciences*, 3(1):22, 2016.

[58] Dominik Schillinger and Martin Ruess. The Finite Cell Method: A review in the context of higher-order structural analysis of CAD and image-based geometric models. *Archives of Computational Methods in Engineering*, 22(3):391–455, 2015.

[59] TM Shih. A procedure to debug computer programs. *International Journal for Numerical Methods in Engineering*, 21(6):1027–1037, 1985.

[60] J Sladek, V Sladek, M Gfrerer, and M Schanz. Mindlin theory for the bending of porous plates. *Acta Mechanica*, 226(6):1909–1928, 2015.

[61] Pavel Solin, Karel Segeth, and Ivo Dolezel. *Higher-order finite element methods*. Chapman and Hall/CRC, 2003.

[62] Arnold Sommerfeld. Die Greensche Funktion der Schwingungsgleichung. *Jahresbericht der Deutschen Mathematiker-Vereinigung*, 21:309–352, 1912.

[63] Larry A Taber. A theory for transverse deflection of poroelastic plates. *Journal of Applied Mechanics*, 59(3):628–634, 1992.

[64] DD Theodorakopoulos and DE Beskos. Flexural vibrations of poroelastic plates. *Acta Mechanica*, 103(1-4):191–203, 1994.

[65] Bert Van Genechten, Dirk Vandepitte, and Wim Desmet. A direct hybrid finite element–wave based modelling technique for efficient coupled vibro-acoustic analysis. *Computer Methods in Applied Mechanics and Engineering*, 200(5):742–764, 2011.

[66] Benjamin Wassermann, Stefan Kollmannsberger, Tino Bog, and Ernst Rank. From geometric design to numerical analysis: A direct approach using the Finite Cell Method on Constructive Solid Geometry. *Computers & Mathematics with Applications*, 2017.

[67] PH Wen and YW Liu. The fundamental solution of poroelastic plate saturated by fluid and its applications. *International Journal for Numerical and Analytical Methods in Geomechanics*, 34(7):689–709, 2010.

[68] Wolfram Research, Inc. *Mathematica, Version 11.1*. Champaign, Illinios, 2017.

[69] Wenchang Zhao, Leilei Chen, Haibo Chen, and Steffen Marburg. An effective approach for topological design to the acoustic–structure interaction systems with infinite acoustic domain. *Structural and Multidisciplinary Optimization*, pages 1–21, 2020.

[70] Olgierd Cecil Zienkiewicz and Robert Leroy Taylor. *The finite element method for solid and structural mechanics*. Butterworth-Heinemann, 2005.